

# MASS OUTFLOW AND CHROMOSPHERIC ACTIVITY OF RED GIANT STARS IN GLOBULAR CLUSTERS II. M13 AND M92

Sz. Mészáros<sup>1,2,3</sup>, A. K. Dupree<sup>1,4</sup> and T. Szalai<sup>2,5</sup>

## ABSTRACT

High resolution spectra of 123 red giant stars in the globular cluster M13 and 64 red giant stars in M92 were obtained with Hectochelle at the MMT telescope. Emission and line asymmetries in  $H\alpha$ , and Ca II K are identified, characterizing motions in the extended atmospheres and seeking differences attributable to metallicity in these clusters and M15. On the red giant branch, emission in  $H\alpha$  generally appears in stars with  $T_{eff} \lesssim 4500$  K and  $\log L/L_{\odot} \gtrsim 2.75$ . Fainter stars showing emission are asymptotic giant branch (AGB) stars or perhaps binary stars. The line-bisector for  $H\alpha$  reveals the onset of chromospheric expansion in stars more luminous than  $\log (L/L_{\odot}) \sim 2.5$  in all clusters, and this outflow velocity increases with stellar luminosity. However, the coolest giants in the metal-rich M13 show greatly reduced outflow in  $H\alpha$  most probably due to decreased  $T_{eff}$  and changing atmospheric structure. The Ca II  $K_3$  outflow velocities are larger than shown by  $H\alpha$  at the same luminosity and signal accelerating outflows in the chromospheres. Stars clearly on the AGB show faster chromospheric outflows in  $H\alpha$  than RGB objects. While the  $H\alpha$  velocities on the RGB are similar for all metallicities, the AGB stars in the metal-poor M15 and M92 have higher outflow velocities than in the metal-rich M13. Comparison of these chromospheric line profiles in the paired metal-poor clusters, M15 and M92 shows remarkable similarities in the presence of emission and dynamical signatures, and does not reveal a source of the ‘second-parameter’ effect.

*Subject headings:* stars: chromospheres – stars: mass loss – stars: AGB and post-AGB – globular clusters: general – globular clusters: individual (M13, M15, M92, NGC 2808)

## 1. Introduction

The well-known second-parameter problem in globular clusters (Sandage & Wildey 1967), in which a parameter other than metallicity affects the morphology of the horizontal branch, re-

---

<sup>1</sup>Harvard-Smithsonian Center for Astrophysics, Cambridge, MA 02138

<sup>2</sup>Department of Optics and Quantum Electronics, University of Szeged, 6701 Szeged, Hungary

<sup>3</sup>e-mail address: meszi@cfa.harvard.edu

<sup>4</sup>e-mail address: dupree@cfa.harvard.edu

<sup>5</sup>e-mail address: szaszi@titan.physx.u-szeged.hu

mains unresolved. Metallicity, as first noted by Sandage & Wallerstein (1960), remains the principal parameter, but pairs of clusters, with the same metallicity, display quite different horizontal branch morphologies thus challenging the canonical models of stellar evolution and leading to the need for a ‘second-parameter’. Cluster ages have been examined in many studies (Searle & Zinn 1978; Lee et al. 1994; Stetson et al. 1996; Lee & Carney 1999; Sarajedini 1997; Sarajedini et al. 1997) and in addition, many other suggestions for the ‘second-parameter(s)’ have been proposed, including: total cluster mass; stellar environment (and possibly free-floating planets); primordial He abundance; post-mixing surface helium abundance; CNO abundance; stellar rotation; and mass loss (Catelan 2000; Catelan et al. 2001; Sills & Pinsonneault 2000; Soker et al. 2001; Sweigart 1997; Buonanno et al. 1993; Peterson et al. 1995; Buonanno et al. 1998; Recio-Blanco et al. 2006). Many authors (VandenBerg et al. 1990; Lee et al. 1994; Catelan 2000) have proposed that the second-parameter problem cannot be explained by only one second parameter. Various studies have attempted to limit the number of second parameters.

An example of paired second-parameter clusters is M15 and M92 ( $[\text{Fe}/\text{H}] = -2.26$  and  $-2.28$  respectively). Although the metallicities of these two clusters are the same (Sneden et al. 2000), their horizontal branches (HBs) differ (Buonanno et al. 1985). M92 has a brighter (by about one magnitude) and redder blue HB extension than M15. The color magnitude diagrams (CMDs) of this pair were examined in detail by Cho & Lee (2007). They found that the difference in the HB morphology between the two is probably not a result of deep mixing in their red giant branch (RGB) sequences, because no significant ‘extra stars’ were found in their observed RGB luminosity functions compared to the theoretical RGB luminosity functions. Sneden et al. (2000) found that Si, Ca, Ti, and Na abundance ratios of the red giants are nearly the same in both clusters, only the  $[\text{Ba}/\text{Ca}]$  ratio shows a large scatter and the mean value in M15 is twice that found in M92. These studies eliminate deep mixing and subtle abundance variations as possible second parameters, while mass loss is examined in this paper. Detailed observations of red giant stars in M15 are contained in Mészáros et al. (2008), but the comparison between M15 and M92 is described here.

M13 ( $[\text{Fe}/\text{H}] = -1.54$ ) is one of the most studied second-parameter globular clusters. M13 and M3 are almost identical in most respects (metallicity, age, chemical composition), but there are dramatic differences in both the HB and blue straggler populations. Analysis of both clusters’ CMDs (Ferraro et al. 1997) with the Hubble Space Telescope revealed that neither age nor cluster density, two popular second-parameter candidates, is likely to be responsible for the differences in these clusters. From the analysis of high-resolution, high signal-to-noise ratio spectra of six RGB stars in M3 and three in M13, Cavallo & Nagar (2000) found that the  $[\text{Al}/\text{Fe}]$  and  $[\text{Na}/\text{Fe}]$  abundances increase toward the tip of the RGB. They concluded that the data for both clusters are consistent with deep mixing as a second parameter. Later, Johnson et al. (2005), from medium-resolution spectra of more than 200 stars in M3 and M13, concurred that deep mixing is the best candidate for second parameter in this pair of clusters. Caloi & D’Antona (2005) also examined the second-parameter problem in M3 and M13 in detail and proposed that the overall difference between M3 and M13 CMD morphologies is due to the different helium content. Since M13 does not have a red

clump in its horizontal branch they suggested that it represents an extreme case of self-enrichment of helium, which might come from the massive asymptotic giant branch stars (AGB) in the first  $\approx 100$  Myr of the cluster life.

A multivariate study of the CMDs for 54 globular clusters was carried out by Recio-Blanco et al. (2006) from Hubble Space Telescope photometry to quantify the parameter dependencies of HB morphology. They found that the total cluster luminosity (therefore the total mass) has the largest impact on the HB morphology, and as Caloi & D’Antona (2005) speculated, there may be enrichment of helium from an earlier population of stars. D’Antona et al. (2002) modeled the evolution of globular cluster stars and showed that different choices of mass–loss rate affect the distribution of stars on the HB.

In this paper we discuss the characteristics of  $H\alpha$  and Ca II K emission in M13 ( $[Fe/H]=-1.54$ ) and M92 ( $[Fe/H]=-2.28$ ). We compare our results with the previously observed, metal-poor cluster M15 ( $[Fe/H]=-2.26$ ) (Mészáros et al. 2008) and the metal-rich cluster NGC 2808 ( $[Fe/H]=-1.15$ ) (Cacciari et al. 2004). Detailed study of these four clusters allows us to examine a possible dependence between the average cluster metallicity and characteristics of  $H\alpha$  and Ca II K emission, and diagnostics of mass outflow. Observations with the same instrument of the second-parameter pair M15 and M92 offer a good comparison to examine mass loss as a possible second parameter.

## 2. Observations and Data Reduction

The Hectochelle on the MMT (Szentgyorgyi et al. 1998) contains 240 fibers that can be placed  $\sim 2$  arcsec apart on the sky across the field of view which spans 1 degree. The diameter of one fiber on the sky is 1.6 arcsec. The apparent diameter of M13 is  $\sim 15$  arc minutes, and about 60–70 red giants in the globular cluster could be measured with each fiber configuration. The apparent diameter of M92 is smaller, and only 30–40 stars could be measured with one configuration. Two separate input fiber configurations for different stars were made for each cluster. A total of 123 different red giant stars in M13 and 64 red giants in M92 were observed in 2006 March and 2006 May.

Targets with a high probability ( $> 95\%$ ) of membership were chosen from the catalog of Cudworth (1976) for M13 and from Cudworth & Monet (1979) for M92. Smooth coverage of the RGB and AGB could be achieved within the constraint of the fiber placement on the sky. The CMD of the observed cluster members can be seen in Figure 1 and the target stars are listed in Table 1 (M13) and Table 2 (M92). Coordinates of the stars were taken from the 2MASS catalog (Skrutskie et al. 2006) and used to position the fibers. Many fibers ( $\sim 150$ – $200$ ) were placed on blank regions of the sky in order to measure the sky background in detail. These sky fibers were equally distributed in the Hectochelle field of view to cover a large area around the clusters. Hectochelle is a single-order instrument and three orders were selected for observation with order-separating filters: OB25 ( $H\alpha$ , region used for analysis  $\lambda\lambda 6475 - 6630$ ), Ca41 (Ca II H&K, region

used for analysis  $\lambda\lambda$  3910 – 3990), and RV31 (region used for analysis  $\lambda\lambda$  5150 – 5300). Bias and quartz lamps for the flat correction were obtained during the afternoon each day. Exposures with the ThAr comparison lamp were obtained before and after every observation during the night to determine the wavelength solution. The spectral resolution was about 34,000 as measured by the FWHM of the ThAr emission lines in the comparison lamp. Exposures in each filter are summarized in Table 3. The number of objects observed changed slightly between observations, because fiber positions need to be reconfigured when targets pass the meridian.

Data reduction was done using standard IRAF spectroscopic packages. The uneven sky intensity in the CCD required special non-standard methods of sky subtraction. These procedures are described in Mészáros et al. (2008).

### 3. Stars with H $\alpha$ Emission

#### 3.1. Determining H $\alpha$ Emission

Two methods have been used for the identification of H $\alpha$  emission. The first selects stars with flux in the H $\alpha$  wings lying above the local continuum. Strong emission can be easily found, however faint emission comparable to the noise of the continuum can be missed. A second method was introduced by Cacciari et al. (2004) and is illustrated in Figure 2. They select a star without emission and the H $\alpha$  absorption line from this star is subtracted from the other spectra. With this method weak emission can be identified, but it strongly depends on the template selected. The H $\alpha$  absorption profile depends on temperature, as well as broadening from turbulent velocity and rotation, both of which could introduce features in the subtracted profile. An individual Kurucz model can be made for every star as a template, and the temperature problem can be avoided, but the uncertainty of other physical parameters can introduce similar effects in the subtracted spectrum. In a continuum-normalized spectrum, the H $\alpha$  emission appears above the continuum level for the majority of stars (L465 and L72 in Figure 2). However in fainter stars only the shape of the H $\alpha$  line profile is changing and the emission does not appear above the continuum, rather just a small additional flux emerges in the absorption wings (L250 and L252 in Figure 2). The identification of this kind of emission can be challenging (L403 in Figure 2). In this paper, we used both methods. However, we selected 8 stars with no emission and of different colors and luminosities to make the template. The stars identified with H $\alpha$  emission are the same with both methods.

No matter which method is used, the detection of faint emission depends on the reduction technique. Continuum normalization and sky subtraction can change the emission flux and move it above or below the continuum level (L252 in Figure 2). Continuum normalization was done using a low-order Chebyshev function in the IRAF task *continuum* in order to fit the continuum and filter throughput. The continuum placement strongly depends on the order of the function and the rejection limits below and above the fit. Sky subtraction is especially challenging with Hectochelle

because additional counts appear between aperture numbers 100 and 150, possibly due to scattered light. This additional flux depends not only on the aperture but also wavelength, and although a reduction system was developed (Mészáros et al. 2008), all sky background cannot be subtracted in the middle section of the CCD. For these reasons the emission of very faint stars can be hard to identify and this can introduce uncertainties in the statistics of the presence of emission.

### 3.2. H $\alpha$ Emission in the CMD

Emission in H $\alpha$  signals an extended and high-temperature chromosphere; in addition the asymmetry of the emission indicates chromospheric mass motions (Dupree et al. 1984; Mauas et al. 2006). We observed a total of 123 different red giant stars in M13 and found 19 with H $\alpha$  emission. In M92, we found 9 stars with H $\alpha$  emission out of 64 objects. Emission above the continuum in the H $\alpha$  profile can be seen in Figures 3 and 4. For comparison, Figure 4 includes a star that exhibits no emission. The color-magnitude diagram (CMD) for each night of observation appears in Figure 5 for both clusters. The intensity ratio, B/R, of Blue (short wavelength) and Red (long wavelength) emission peaks for stars showing emission is contained in Table 4.

In M13, emission is found in stars brighter than  $V=14.69$ , corresponding to  $M_V = +0.21$ , using the apparent distance modulus  $(m - M)_V = 14.48$  from Harris (1996). The star which marks the faint luminosity limit (L719) appears to be either a blend, or a physical binary RGB star judging from its position in the CMD (bluer than RGB stars at the same absolute magnitude). This star also had a significant radial velocity change between observations (see Section 4.1). Among the RGB stars, L1073 at  $V=12.88$  ( $M_V = -1.60$ ) marks the faint luminosity limit of H $\alpha$  emission. Stars brighter than this are on the RGB or AGB; the evolutionary status cannot be determined from the CMD itself. Stars in M92 that show emission are brighter than  $V=14.54$  ( $M_V = -0.1$ ), using the apparent distance modulus  $(m - M)_V = 14.64$  from Harris (1996). However the faintest star (IX-12) showing emission appears to be an AGB star, according to its position in the CMD. Considering stars on the RGB, the star IV-94 ( $V=13.06$ ,  $M_V = -1.58$ ) appears to be the faintest RGB star showing emission in M92 (although the differences between the RGB and AGB at that part of the CMD are very small). In M15, the faint luminosity limit showed significant changes between observations; this amounted to a change in the faint magnitude limit of 0.79 magnitudes (Mészáros et al. 2008). One can assume that the emission behaves very similarly in these clusters as well, and that the faint luminosity limit of H $\alpha$  emission is not constant.

For comparison on a luminosity scale, unreddened colors for M13 and M92 stars were calculated. Foreground reddening [ $E(B - V) = 0.02$  for both clusters] and the apparent distance modulus were taken from Harris (1996). The effective temperatures, bolometric corrections, and luminosities were obtained from the  $V - K$  colors (Tables 5 and 6) using the empirical calibrations by Alonso et al. (1999, 2001) and the cluster average metallicity [Fe/H]= $-1.54$  for M13, [Fe/H]= $-2.28$  for M92 (Harris 1996). Thus on the red giant branch alone, emission appears in stars brighter than  $\log(L/L_\odot) = 2.79$  in M13 and  $\sim 78\%$  of these stars (18) show H $\alpha$  emission. In M92 this luminosity

limit is slightly lower than in M13,  $\log(L/L_{\odot}) = 2.74$ , and also  $\sim 78\%$  of these stars (7) show emission.

Although both clusters were observed on two different days, the configurations were chosen to eliminate stars already observed in order to achieve full coverage of stars in the CMD. When it was possible, previously observed stars were configured to the remaining fibers, but the number of stars observed twice for both clusters is very small, only 17 in M13 and 15 in M92. Of the stars showing  $H\alpha$  emission, comparison was possible for only two stars in M13 and three stars in M92. In M13, between 2006 March 14 and 2006 May 10, L72 changed asymmetry (see Figure 3), while for the other star, L719, the already weak emission vanished. In M92, all three stars (II-53, VII-18, and IX-12) kept the same emission asymmetry, but the flux level of IX-12 changed in only two days (see Figure 4).

## 4. Radial Velocities

### 4.1. Cross-correlation Technique

To measure accurate radial velocities, we chose the cross-correlation method using the IRAF task *xcsao*. Two filter regions, OB25 and RV31, were used for radial velocity measurements. The spectral region on the RV31 filter between 5150 Å and 5300 Å contains several hundred narrow photospheric absorption lines of predominantly neutral atoms and very few terrestrial lines, thus the cross-correlation function is narrower than from the  $H\alpha$  region, which only contains  $\sim 10$  lines (Figure 6). In the OB25 filter, the region selected for the cross-correlation spanned 6480 Å to 6545 Å purposely omitting the  $H\alpha$  line. This results in 100–200  $\text{m s}^{-1}$  errors with the RV31 filter as compared to 200–400  $\text{m s}^{-1}$  using the wavelength region earlier described in the  $H\alpha$  filter. Spectra of our targets from both filters were cross-correlated against 2280 spectra calculated by Coelho et al. (2005) covering temperatures between 3500 and 7000 K, metallicities between  $[\text{Fe}/\text{H}] = -2.5$  and  $+0.5$ , and  $\log g$  between 0 and 5. Radial velocities were corrected to the solar system barycenter. To calculate the radial velocity of a star, the radial velocities from ten templates with the highest amplitude of the cross-correlation function for each filter were collected and averaged together. A sample of the template spectra compared to an observation can be seen in Figure 6. The physical parameters of the templates that were used for the radial velocity measurements usually agreed with each other within 200 K in temperature, 1 in  $\log g$ , and  $-0.5$  in  $[\text{Fe}/\text{H}]$  with our calculated physical parameters (Tables 5 and 6). For almost every star the radial velocity differences among the 10 highest correlation templates in each filter were less than  $0.5 \pm 0.2 \text{ km s}^{-1}$ , which is close to the error of the individual measurements.

We compare our results with those found in the literature. In M13, Soderberg et al. (1999) used the Hydra spectrograph on the 4–m Mayall telescope to obtain spectra of 150 stars. Their template for the cross-correlation was an averaged spectrum of all giants for each Hydra observation. Therefore the individual radial velocities were determined as compared to the average cluster

velocity. The radial velocity of the averaged spectrum was calculated by cross-correlating it to the solar spectrum. Comparison of the results can be seen in Figure 7. Errors spanned  $0.5 \text{ km s}^{-1}$  to  $3\text{--}5 \text{ km s}^{-1}$  in their sample, and there is a systematic  $1.1 \pm 0.5 \text{ km s}^{-1}$  offset (Figure 7, left upper panel) between our radial velocities and those of Soderberg et al. (1999). Hectochelle velocities determined using the  $\text{H}\alpha$  region from 2006 March 14 agreed with the observations two days later with the RV31 filter (see Figure 7, left lower panel) for the same stars. Radial velocities calculated from the data taken with the RV31 filter in 2006 May also agreed with data taken with the OB25 filter on 2006 March 14 (Figure 8, right upper and lower panel). We find the average radial velocity of M13 to be  $-243.5 \pm 0.2 \text{ km s}^{-1}$ , which is slightly lower than the cluster radial velocity ( $-245.6 \pm 0.3 \text{ km s}^{-1}$ ) quoted in the Harris (1996) catalog.

Five stars observed with Hectochelle in M13 were reported as possible binaries by Shetrone (1994), when the radial velocities measured with the 3-m Shane telescope (Lick Observatory) were compared with velocities determined by Lupton et al. (1987). In all of these stars, differences between the two observations were larger than  $4 \text{ km s}^{-1}$  which exceeds the measurement errors of  $\sim 1 \text{ km s}^{-1}$  and may reflect intrinsic stellar variability or binary reflex motions. Our radial velocities differ by  $4\text{--}5 \text{ km s}^{-1}$  compared with Lupton et al. (1987), but agree within  $1\text{--}2 \text{ km s}^{-1}$  with Shetrone (1994), which also suggests that long-term changes are present. Among these five stars, we observed one, L72, which showed  $2.1 \text{ km s}^{-1}$  velocity change between 2006 March and 2006 May. Lupton et al. (1987) identified this star in M13 as a possible binary from variations in radial velocity over several years of observations. L72 is also known as a pulsating variable star with a possible period of 41.25 days (Russeva & Russev 1980), so the velocity change found here may also relate to pulsation. L719, which marks the faint luminosity limit of stars showing  $\text{H}\alpha$  emission, also had radial velocity changes <sup>1</sup> between 2006 March 14 to 2006 May 10 from  $-254.1 \pm 0.3 \text{ km s}^{-1}$  to  $-245.2 \pm 0.2 \text{ km s}^{-1}$ . No other stars showed significant, larger than  $2 \text{ km s}^{-1}$ , variations in our sample in M13.

A large sample of stars in M92 was observed by Drukier et al. (2007) using the HYDRA multi-fiber spectrograph on the 3.5-m WIYN telescope. Their errors spanned  $0.3\text{--}1.2 \text{ km s}^{-1}$ . The comparison of results can be seen in Figure 8. Radial velocities for the same stars agreed within the errors (Figure 8, left upper panel). The Hectochelle spectra give the cluster average radial velocity as  $-118.0 \pm 0.2 \text{ km s}^{-1}$ , which is lower than the value ( $-120.3 \pm 0.1 \text{ km s}^{-1}$ ) quoted in the Harris (1996) catalog. In M92, two stars show radial velocity variations, which usually indicates binarity or pulsation. II-53 had a significant velocity variation of  $7.7 \text{ km s}^{-1}$  between 2006 May 7 and 2006 May 9. Another star, XI-38, showed a  $4.9 \text{ km s}^{-1}$  difference between the radial velocity measured by Drukier et al. (2007) and the velocity measured by us on 2006 May 7.

---

<sup>1</sup>If this object were a single line binary, the velocity change allows only lower limits to the period ( $P > 90$  days) and semi-major axis ( $a \gtrsim 10R_*$ ). The putative companion to the red giant could be either a white dwarf or a late main sequence star, and probably the former since the color is bluer than a red giant.

## 4.2. Bisector of H $\alpha$ Lines

To search for mass motions in the chromosphere, we evaluated the H $\alpha$  core asymmetry using a bisector method. The difference between the center of the line core and the line center near the continuum level gives a measure of the atmospheric dynamics through the chromosphere. To accomplish this, the line profile with continuum normalization was divided into 20 sectors. The top sector was usually between 0.7 and 1.0 of the continuum in the normalized spectrum, the lowest sector was placed 0.01 – 0.05 above the deepest part of the line depending on its signal-to-noise ratio. The velocities of the H $\alpha$  bisector asymmetry ( $v_{bis}$ ) are calculated in the following way: the top and the bottom 3 sectors are selected, the wavelength average of each sector is calculated, then subtracted one from another and changed to a velocity scale. The bisector velocities,  $v_{bis}$ , are shown in Figure 9 and listed in Tables 7 and 8. A negative value corresponds to an outflowing velocity. The error of the majority of the measurements spanned 0.5–1.0 km s<sup>-1</sup>; only stars fainter than V=15 magnitude exceeded 1.0 km s<sup>-1</sup> in measurement error. RGB stars fainter than  $\log(L/L_{\odot}) = 2.5$  did not show asymmetry in the H $\alpha$  core and  $v_{bis}$  was nearly zero. This luminosity is nearly the same for both clusters and also very similar to M15 (Mészáros et al. 2008), which suggests that the luminosity limit of the line core asymmetry marking the onset of expansion does not depend on average cluster metallicity. Stars brighter than  $\log(L/L_{\odot}) = 2.5$  showed core asymmetry and the majority of the bisectors were blue shifted. The start of chromospheric outflow presumably relates to mass loss. However, the value of  $v_{bis}$  appears to depend on luminosity. In the metal-rich cluster M13,  $v_{bis}$  increases with luminosity and reaches its maximum value ( $\approx 5$  km s<sup>-1</sup>) at about  $\log(L/L_{\odot}) = 3.2$  but the most luminous stars exhibit lower (near zero km s<sup>-1</sup>) values. In the more metal-poor cluster M92,  $v_{bis}$  also increases with luminosity and reaches the maximum value at  $\log(L/L_{\odot}) = 3.4$  but the decrease in outflow velocity is much smaller. At the same luminosity,  $T_{eff}$  for the metal-rich M13 giants is lower than for M92. Thus, the apparent decrease in  $v_{bis}$  at high luminosity would appear to be related to the changing atmospheric structure (see Section 6.1).

Where AGB stars are well separated in color from the RGB stars in M92, the AGB stars exhibit larger values of  $v_{bis}$  than RGB stars (Figure 10). The star IX-12 in M92 shows the largest bisector velocity at  $v_{bis} = -15.9 \pm 1.3$  km s<sup>-1</sup>, and this star is the faintest star showing emission in the cluster (see Figure 9). Its position in the CMD suggests that this star is an AGB star (Figure 5). AGB stars in M13 generally have lower bisector velocities than AGB stars in M92 which suggests that the metal-rich objects have slower winds.

## 5. Ca II K Profiles

Spectra in the Ca II H&K region were obtained for 119 red giant stars in M13 and 63 red giants in M92. The profiles of the Ca II K core ( $\lambda 3933$ ) are shown in Figures 11 and 12 for all stars exhibiting emission. The position of these stars in the CMD can be seen in Figure 13. The intensity



ratio of the emission core,<sup>2</sup> B/R, is summarized in Table 9. Because of the high radial velocity of M13 ( $v_{rad}=-243.5$  km s<sup>-1</sup>), absorption by the local interstellar medium (ISM) is well away from the Ca II K core. Although the ISM is closer to the Ca II K emission in M92 ( $v_{rad}=-118.0$  km s<sup>-1</sup>), it does not affect the emission profile. Red giant stars have low flux levels near 3950 Å, hence the deep photospheric absorption in Ca II H&K causes the photon noise to become comparable to the flux of the core emission for stars fainter than 14th magnitude. Determining the presence of emission is challenging. The spectra of our targets were compared to a Kurucz model, [computed by Coelho et al. (2005) without a chromosphere], to verify the emission. Altogether 34 stars showed Ca II K emission in M13 and 12 in M92.

The spectra of H $\alpha$  and Ca II were obtained on the same night or separated by 1 or 2 days, and the asymmetry of the K-line emissions is similar to that found in H $\alpha$  for the majority of the stars. The brightest stars in M13 showed stronger Ca II K emission than stars in M92 at the same luminosity. This results because the lower effective temperatures of M13 giants increase the contrast of the emission to the continuum. For stars fainter than V=14, the ratio of the blue to the red side of the Ca II K emission core, or even the presence of the emission is difficult to determine.

The velocity of the central reversal (K<sub>3</sub>) was measured for the brightest stars (Table 10) using three strong absorption lines closest to Ca II K as a photospheric reference. A Gaussian function using the IRAF task *splot* was fitted to the cores of the photospheric lines and the central reversal absorption of Ca II K. Radial velocities of the photospheric lines were averaged and then subtracted from the radial velocity of the Ca II K<sub>3</sub> feature. The velocity shift of the K<sub>3</sub> absorption lies between 0 km s<sup>-1</sup> and -16 km s<sup>-1</sup> (Table 10).

## 6. Discussion

In this paper and in our previous study (Mészáros et al. 2008), we have presented H $\alpha$  and Ca II K spectroscopy of 297 red giants in 3 globular clusters with different metallicities (Harris 1996): M13 ([Fe/H]=-1.54), M15 ([Fe/H]=-2.26), and M92 ([Fe/H]=-2.28). The presence of emission in these transitions signals an extended, high-temperature chromosphere, and the asymmetry of the emission and the line core indicates chromospheric mass motions. Comparison of the statistics of the profile characteristics among the globular cluster stars could reveal the effects of metallicity on mass loss. In the following sections, we discuss several characteristics of the presence of H $\alpha$  and Ca II emission and the resulting velocity signatures. Parameters of the clusters and the lines can be found in Table 11. In the final section of the Discussion, we compare our results with those of Cacciari et al. (2004) who presented similar line profiles for 137 red giants in the globular cluster NGC 2808.

---

<sup>2</sup>B signifies the short-wavelength emission peak and R the long-wavelength emission peak.

### 6.1. Presence of H $\alpha$ Emission

On the RGB, H $\alpha$  emission sets in for all stars with  $T_{eff} \lesssim 4500$  K and  $\log(L/L_{\odot}) \gtrsim 2.75$  in all 3 clusters: M13, M15,<sup>3</sup> and M92. It is perhaps fortuitous that the limits are so similar since the presence of H $\alpha$  can change by as much as 0.79 magnitudes from observations on one date to another (Mészáros et al. 2008). Stars on the AGB show H $\alpha$  emission to lower luminosity limits than the RGB objects. The faint limits of emission for AGB stars in M13 and M92 are comparable, while AGB stars in M15 with emission are brighter. Emission is variable in all giants and again there does not appear to be a systematic dependence of luminosity limits on metallicity. This result suggests that whatever mechanism produces the variable emission occurs similarly in all metal-poor red giants.

The percentage of stars showing inflow and outflow in the H $\alpha$  emission wings<sup>4</sup> varies from cluster to cluster and appears to be related to cluster metallicity. In the metal-poor M92, about 82% of stellar spectra showing emission have an inflow signature (18% show outflow) and the study of M15 (Mészáros et al. 2008) revealed that about 78% of stars with H $\alpha$  emission displayed an inflow signature (22% outflow). These two clusters show similar behavior in their chromospheric dynamics. M13 has a more equal distribution of the dynamical signature with 55% of the H $\alpha$  spectra indicating inflow (45% outflow). Since all the luminous stars are losing mass, it might be puzzling why the dominant emission signature in H $\alpha$  is one of inflow. (And as discussed in the following section, the line cores generally indicate outflow.) We believe this relates to the dynamics of the atmosphere. It appears likely that our targets are pulsating (Mayor et al. 1984), and comparison with the well-known pulsators, Cepheids, shows that inflow signatures in H $\alpha$  are accompanied by inflow in the metallic photospheric lines (Baldry 1997), and that inflow occurs for a larger fraction of the pulsation period in longer period Cepheids than in shorter period stars (Nardetto et al. 2006; Petterson et al. 2005). In this way, we understand the dominance of inflow emission signatures. The different proportions of inflow/outflow signatures may indicate that the pulsation period in M15 and M92 is generally longer than in M13. It is clear that variability is ubiquitous. Almost all stars brighter than  $V=12.5$  are variables in M13, but only one variable red giant exhibits periodic photometric variations, and the remaining ones are semi-regular or irregular (Kopacki et al. 2003).

The fraction of stars showing H $\alpha$  emission increases with luminosity and decreasing effective temperature. Because of the separation of red giant branches in the CMD due to metallicity, the distribution of the emission with luminosity and effective temperatures differs between clusters. At the same luminosity, the metal rich M13 exhibits more stars with H $\alpha$  emission than the metal poor M92 or M15, because the effective temperatures are lower in M13 for a constant luminosity.

---

<sup>3</sup>In M15, the stars K672 and K875 are clearly AGB objects, and the faintest RGB star showing emission in that study is B30.

<sup>4</sup>As measured by the ratio of B/R – the short wavelength to long wavelength peaks of the H $\alpha$  emission wings.

However, at the same stellar effective temperature, M15 and M92 exhibit more stars showing emission than M13. This may appear as a metallicity effect, but it originates in the fact that both high luminosity and low effective temperature produce more H $\alpha$  emission.

## 6.2. The H $\alpha$ Bisector Velocity

Stars brighter than  $\log (L/L_{\odot}) = 2.5$  show a blue-shifted H $\alpha$  core in both M13 and M92, and outflows become faster with increasing luminosity (Figure 9). This occurs in M15 as well (Mészáros et al. 2008). Thus, the luminosity at the onset of outflow, indicated by the H $\alpha$  line core is independent of metallicity. The behavior of the bisector velocity on the RGB changes at the highest luminosities (Figure 14). Giants in M13, the most metal-rich cluster, show lower bisector velocities in the most luminous (and coolest stars). In fact, the velocities of the H $\alpha$  core approach  $0 \text{ km s}^{-1}$  with respect to the photosphere, signaling that the outward motions have decreased in the atmospheric region where the H $\alpha$  line forms. Since the brightest stars in M13 have a lower  $T_{eff}$  than those in M15 and M92 (Fig. 14), we suspect that the decrease in the H $\alpha$  bisector velocity results from the changing structure of the very extended atmosphere. The H $\alpha$  wing asymmetry and Ca II K asymmetry preponderantly signal outflow in the most luminous stars. It is noteworthy that outflow begins at a luminosity,  $\log (L/L_{\odot}) \sim 2.5$ , and as the stars become more luminous, emission wings occur in the H $\alpha$  profile in our sample at  $\log (L/L_{\odot}) \sim 2.75$ . We conjecture that the onset of pulsation marked by the observed outward motion leads to a warmer chromosphere producing emission wings in H- $\alpha$ .

Differences in the coreshift between AGB and RGB stars can be seen where these stars are distinct on the CMD. Stars on the AGB, between  $\log (L/L_{\odot}) = 2.0$  and 2.7, showed slightly larger bisector velocities than RGB objects in both clusters, although the values are most extreme in M92. AGB stars tend to have lower values of  $\log g$  and smaller escape velocities in the chromosphere as compared to RGB stars, which makes them more sensitive to mass loss driving mechanisms resulting in faster winds. We can speculate that there is more heating in the hotter AGB stars; it may be that a putative magnetic field is stronger after the stars have been through helium burning enabling enhanced wave motions, heating, and acceleration in the chromosphere as compared with RGB stars. The extremes of outflow velocity on the AGB tend to be larger in the metal-poor clusters, M15 and M92, than in M13 (see Figure 10 and 14).

There is no evidence here that the outflow velocity is slower at low metallicity. This suggestion resulted from observations of OH/IR stars in the low metallicity Magellanic Clouds (Marshall et al. 2004), and modeling of dust driven winds (Helling 2000; Wachter et al. 2008) such as those identified in Omega Centauri by Spitzer Space Telescope observations (Boyer et al. 2008; McDonald et al. 2009). In fact, we find just the opposite. M15 and M92 have generally higher velocities than stars in M13 (see Figure 14, lower panels). No evidence for a ‘super-wind’ (Renzini 1981; Bowen & Willson 1991) in the sense of an abrupt high velocity outflow is present in our spectra, although the largest mass-loss rates might be expected for stars with lower  $T_{eff}$  than found in this sample (Wachter et al.

2002). Even in the dusty red giants in M15 detected with the Spitzer Space Telescope (Boyer et al. 2006), the bisector velocities have similar values as red giants without an IR excess (Mészáros et al. 2008). These similarities suggest that mass loss and dust production are not correlated, and the triggering of dust production may be an episodic phenomenon.

Three stars in M13 exhibit large ( $>2 \text{ km s}^{-1}$ ) bisector-velocity changes between observations. The star at the lowest luminosity limit, L719, shows a  $4.7 \text{ km s}^{-1}$  bisector velocity difference, which is clearly visible on the spectrum (see Fig. 3) as the  $\text{H}\alpha$  emission disappeared. K342 and K658 showed  $2.2 \text{ km s}^{-1}$  and  $4.9 \text{ km s}^{-1}$  changes respectively, but these stars are faint and the error due to the low signal-to-noise of the spectra is comparable to the velocity change. In M92, only 2 stars show a large coreshift in  $\text{H}\alpha$ : II-6 is a very faint star and this difference is comparable to the error of our measurements; IX-12 is an AGB star and shows similar  $v_{bis}$  values as stars of the same luminosity. However between our 2 observations separated by 2 days, the coreshift changes for other stars are relatively small. In M15 (Mészáros et al. 2008), it is the AGB stars in the  $\log(L/L_{\odot}) = 2.3 - 3.0$  luminosity region that show large bisector velocity changes ( $3-7 \text{ km s}^{-1}$ ) over a time span of one year or more.

On the RGB, the velocities in M15 indicate that systematic outflow (more negative than  $-2 \text{ km s}^{-1}$ ) in the  $\text{H}\alpha$  core occurs at luminosities,  $\log(L/L_{\odot}) \gtrsim 2.5$ . The velocity of the outflow increases with luminosity and only the brightest stars show slightly smaller outflow (Figure 9 and 14). In M92, which is also very metal-poor, stars brighter than  $\log(L/L_{\odot}) = 2.5$  showed bisector velocities more negative than  $-2 \text{ km s}^{-1}$ , and only the brightest star shows smaller outflow velocities. If there are differences in mass loss between M15 and M92, the shapes of the  $\text{H}\alpha$  line profiles do not reflect this. Thus the  $\text{H}\alpha$  line by itself cannot help to decide if mass loss is the ‘second parameter’ in M15 and M92. McDonald & van Loon (2007) found no significant correlation between core asymmetry and luminosity, when they examined  $\text{H}\alpha$  and Ca II IR triplet spectra of 47 red giant stars near the RGB tip in 6 globular clusters. Above a certain luminosity the bisector velocity of  $\text{H}\alpha$  becomes small and motions are difficult to detect in this region of the atmosphere, independent of cluster metallicity. Possibly another diagnostic such as He I  $\lambda 10830$  or ultraviolet lines, formed higher in the atmosphere needs to be examined. A He I  $\lambda 10830$  absorption line was detected (Smith et al. 2004) in the star L687 in M13, with an extension to  $-30 \text{ km s}^{-1}$ , suggesting that when the helium line becomes detectable (apparently for  $T_{eff} \sim 4650 \text{ K}$ ), it can give an indication of a faster wind. This He I  $\lambda 10830$  velocity is comparable to the higher values of the  $\text{H}\alpha$  bisector velocities that are found here in AGB stars. Pilachowski et al. (1996) classifies L687 as an AGB star.

### 6.3. The Ca II Emission and Velocity

The Ca II  $\text{K}_2$  emission appears at lower luminosities than  $\text{H}\alpha$  emission in both clusters [ $\log(L/L_{\odot}) = 1.92$  for M13 and  $\log(L/L_{\odot}) = 1.96$  for M92]. In M15 (Mészáros et al. 2008) the Ca II K luminosity limit agrees with the  $\text{H}\alpha$  emission limit [ $\log(L/L_{\odot}) = 2.36$ ], but the low

signal-to-noise ratio of those observations did not allow us to determine the presence of Ca II H&K emission in fainter stars. The lower luminosity limit of Ca II K emission does not appear to be dependent on the cluster metallicity.

The number of stars with Ca II emission in both M13 and M92 exceeds the number of stars showing H $\alpha$  emission. Stars with H $\alpha$  emission generally have Ca II K emission, but not all stars with Ca II K emission show H $\alpha$  emission. This difference is not unexpected since the regions of formation of the Ca II K core and the H $\alpha$  emission wings are separated in the atmosphere of a giant. Models suggest that Ca II K emission forms lower in the atmosphere than H $\alpha$  wings (Dupree 1986). Additionally H $\alpha$  shows variations in asymmetries over the span of a few days (Cacciari & Freeman 1983; Mészáros et al. 2008) which could contribute to the differences. Some stars in both clusters were observed twice at Ca II. Changes in Ca II K emission were observed in two stars in M13 and four stars in M92 where the line profile of Ca II K, either changed asymmetry or the emission strengthened or weakened, or both.

The outflow velocities of the Ca II K<sub>3</sub> reversal are generally larger than the bisector velocities of the H $\alpha$  line for the same stars (Figure 9). Similar behavior was found by Zarro & Rodgers (1983) in Population I giants and supergiants, and they concluded from the similarity of line profiles that Ca II K line is formed higher in the atmosphere and the increased outward velocity reflects a mass-conserving outflow. While models of the Sun suggest that the Ca II K<sub>3</sub> feature forms in a higher atmospheric region than the core of the H $\alpha$  line (Avrett 1998), some chromospheric models of metal-deficient giants (Dupree 1986; Mauas et al. 2006) locate the approximate depth of formation of the Ca II K<sub>3</sub> feature below that of the H $\alpha$  core. These models would suggest the opposite conclusion from Population I stars, that the flow is decelerating in the upper atmosphere. Yet another model (Dupree et al. 1992) for the metal-deficient giant HD 6833 finds the contribution function of Ca II K<sub>3</sub> to lie above that of the H $\alpha$  core and hence signal an accelerating outflow. Some ambiguity may exist in the definition of the region of formation, and in addition it can extend over a substantial height in the chromosphere. In some cases, the He I  $\lambda$  10830 line, clearly formed above both Ca II K and H $\alpha$  shows even higher outflow velocities in metal-deficient stars (Dupree et al. 1992; Smith et al. 2004), so the accelerating outflow models appear preferable.

#### 6.4. Comparison to NGC 2808

Red giants in another metal rich cluster, NGC 2808, were studied by Cacciari et al. (2004) and can be compared to M13. However, this comparison may be somewhat compromised since NGC 2808 has an extreme case of peculiar horizontal branch morphology (Lee et al. 2005) and a split main sequence with potentially 3 populations (Piotto et al. 2007), making it one of the most persuasive clusters for the existence of possible multiple stellar populations including a super helium-rich component (Lee et al. 2005; D’Antona & Caloi 2008). These features of NGC 2808 make it quite different from M13 – the metal rich cluster in our sample. M13 has a more chemically homogeneous population, although it is conjectured to consist of predominantly second generation

stars (D’Antona & Caloi 2008). The average metallicity of NGC 2808 ( $[\text{Fe}/\text{H}]=-1.15$ ) is higher than M13 ( $[\text{Fe}/\text{H}]=-1.54$ ), by a factor of 2.5.

The detection threshold for  $\text{H}\alpha$  emission on the RGB in NGC 2808, of  $\log(L/L_{\odot}) = 2.5$  is fainter by  $\sim 0.2$  magnitudes than the limits for M13, M15, and M92 (see Table 11). Since the appearance of emission in the  $\text{H}\alpha$  line varies with time, these limits are comparable, one with another. However, the percentage of red giants exhibiting emission is less at 52% than we find for M13, M15, and M92 where the value is about 80%. The atmospheres of the NGC 2808 giants may be at lower temperatures since, for the same input energy, radiation losses are greater due to the increased abundance of metals than in metal-poor objects.

Differences arise in the  $\text{H}\alpha$  outflow signature indicated by the emission wings in NGC 2808 where an exceptionally low percentage (at 7%) is found by Cacciari et al. (2004) in contrast to the 45% of red giants showing outflow in M13 and 18–22% in the metal-poor clusters, M15 and M92.

Cacciari et al. (2004) measured significant core shifts ( $< -2 \text{ km s}^{-1}$ ) of  $\text{H}\alpha$  in 7 stars of their sample of giants in NGC 2808. These stars are brighter than  $\log(L/L_{\odot}) = 2.9$ . It is interesting that the 3 most luminous stars in their sample had core shifts of  $1 \text{ km s}^{-1}$  or less, similar to our results for M13 (Figure 9). M4, another cluster of similar metallicity as NGC 2808 also did not have coreshifts (more negative than  $-2 \text{ km s}^{-1}$ ) either in  $\text{H}\alpha$  or Na D in any of  $\approx 10$  stars that have luminosities  $\log(L/L_{\odot}) > 3.3$  (Kemp & Bates 1995).

The luminosity limit in NGC 2808 (Cacciari et al. 2004) for Ca II K emission lines is  $\log(L/L_{\odot}) \sim 2.6$  which is higher than the  $\text{H}\alpha$  limit in NGC 2808. This result is puzzling since Ca II K is found at lower luminosities than  $\text{H}\alpha$  emission in the other clusters, M13, M15, and M92. The resolution of the Calcium spectra studied by Cacciari et al. (2004) was the lowest of all their spectra at  $R=19600$ , and the signal-to-noise in the line core for the brightest stars was only 15. So it is possible that Calcium was not detected in the fainter targets. The limit for Ca II K in NGC 2808 is  $\sim 0.2$  magnitudes brighter than found in M15 which is a metal-poor cluster. The 2 metal poor clusters, M15 and M92 differ in the Ca II K limit by 0.4 magnitudes. At present, there is not sufficient evidence to claim that the B/R ratio of Ca II K emission varies night to night as the B/R ratio of  $\text{H}\alpha$  emission. The core shift of Ca II K in NGC 2808 is generally more negative than the value for  $\text{H}\alpha$ , similar to that found here for the most luminous stars (Figure 9).

Since both the  $\text{H}\alpha$  emission and emission wing asymmetries are variable, it is difficult to draw firm conclusions about systematic differences between clusters. In the sample of red giants in NGC 2808 studied by Cacciari et al. (2004), a lower fraction of stars was found with  $\text{H}\alpha$  emission and with outflow signatures in the emission wings than in the more metal-poor clusters (M13, M15, M92). However, the dynamical characteristics including the luminosity onset of outflow and wind speeds, appear indistinguishable among these clusters.

## 7. Conclusions

Summarizing, we find the following:

1. Hectochelle spectra of M13, M15, and M92 show  $H\alpha$  emission to occur on the red giant branch in stars with  $T_{eff} \lesssim 4500$  K and  $\log(L/L_{\odot}) \gtrsim 2.75$ . AGB stars exhibit  $H\alpha$  emission to lower luminosities. Ca II K emission extends to lower luminosities than  $H\alpha$  both on the RGB and AGB.

2. Considering 3 clusters, spanning  $[Fe/H]=-1.54$  (M13), to  $[Fe/H]=-2.3$  (M15, M92), we find no *systematic* dependence of the presence of  $H\alpha$  or Ca II K emission from red giants on  $T_{eff}$ ,  $L/L_{\odot}$ , or cluster metallicity.

3. Asymmetric  $H\alpha$  cores show that chromospheric material is flowing out from stars brighter than  $\log(L/L_{\odot}) \sim 2.5$  and the speed of the outflow increases with increasing stellar luminosity. This outflow may represent the onset of mass loss, and the luminosity at which outflow begins is similar for all metallicities.  $H\alpha$  velocities on the red giant branch are similar for all metallicities (but not for AGB stars, see below).

4. Stars on the asymptotic giant branch near  $\log(L/L_{\odot}) \sim 2.0 - 2.7$  show higher outflow velocities than RGB stars, and faster outflows are found in the metal-poor M15 and M92 than the metal-rich M13 objects.

5. The sensitivity of  $H\alpha$  to mass motions decreases for  $T_{eff} < 4000$  K causing the coolest giants in M13 to exhibit little or no outflow in this line.

6. The Ca II  $K_3$  absorption features exhibit higher velocities than  $H\alpha$  suggesting accelerating outflows in the chromospheres.

7. We find no differences in chromospheric signatures in the profiles or the presence of  $H\alpha$  and Ca II that can resolve the 'second-parameter' problem for the paired clusters, M15 and M92.

We thank the referee for very detailed comments that significantly improved the presentation. Observations reported here were obtained at the MMT Observatory, a joint facility of the Smithsonian Institution and the University of Arizona. We are grateful to the scientists at CfA who are developing and characterizing Hectochelle: Nelson Caldwell, Daniel G. Fabricant, Gábor Fűrész, David W. Latham, and Andrew Szentgyorgyi. The authors also would like to thank John Roll and Maureen A. Conroy for developing SPICE software, and Mike Alegria, John McAfee, Ale Milone, Michael Calkins and Perry Berlind for their help during the observations. Kyle Cudworth kindly provided coordinates and photometry for M13 and M92 stars. Szabolcs Mészáros is supported in part by a SAO Predoctoral Fellowship, NASA, and the Hungarian OTKA Grant TS049872, T042509 and K76816. This research is also supported in part by the Smithsonian Astrophysical Observatory.

## REFERENCES

- Alonso, A., Arribas, S., & Martínez-Roger, C. 1999, *A&AS*, 140, 261
- Alonso, A., Arribas, S., & Martínez-Roger, C. 2001, *A&A*, 376, 1039
- Arp, H. C. 1955, *AJ*, 60, 317
- Avrett, E. H., 1998, *Solar Electromagnetic Radiation Study for Solar Cycle 22*, ed. J. M. Pap, C. Frölich, & R. K. Ulrich, (Dordrecht:Kluwer), p. 449
- Baldry, I. K., Taylor, M. N., Bedding, T. R., & Booth, A. J. 1997, *MNRAS*, 289, 979
- Bowen, G. H., & Willson, L. A. 1991, *ApJ*, 375, L53
- Boyer, M. L., McDonald, I., van Loon, J. T., Woodward, C. E., Gehrz, R. D., Evans, A., & Dupree, A. K. 2008, *AJ*, 135, 1395
- Boyer, M. L., Woodward, C. E., van Loon, J. T., Gordon, K. D., Evans, A., Gehrz, R. D., Helton, L. A., & Polomski, E. F. 2006, *AJ*, 132, 1415
- Buonanno, R., Corsi, C. E., & Fusi Pecci, F. 1985, *A&A*, 145, 97
- Buonanno, R., Corsi, C. E., Fusi Pecci, F., Richer, H. B., & Fahlman, G. G. 1993, *AJ*, 105, 184
- Buonanno, R., Corsi, C. E., Pulone, L., Fusi Pecci, F., & Bellazzini, M. 1998 *A&A*, 333, 505
- Cacciari, C. et al. 2004, *A&A*, 413, 343
- Cacciari, C., & Freeman, K. C. 1983, *ApJ*, 268, 185
- Caloi, V., & D'Antona, F. 2005, *A&A*, 435, 987
- Catelan, M. 2000, *ApJ*, 531, 826
- Catelan, M., Bellazzini, M., Landsman, W. B., Ferraro, F. R., Fusi Pecci, F., & Galletti, S. 2001, *AJ*, 122, 3171
- Cavallo, R. M., & Nagar, N. M. 2000, *AJ*, 120, 1364
- Cho, D. H., & Lee, S. G. 2007, *AJ*, 133, 2163
- Coelho, P., Barbuy, B., Meléndez, J., Schiavon, R. P., & Castilho, B. V. 2005, *A&A*, 443, 735
- Cohen, J. G. 1976, *ApJ*, 203, L127
- Cudworth, K. M. 1976, *AJ*, 81, 975
- Cudworth, K. M., & Monet, D. G. 1979, *AJ*, 84, 774



- D'Antona, F., Caloi, V., Montalbán, J., Ventura, P., & Gratton, R. 2002, *A&A*, 395, 69
- D'Antona, F., & Caloi, V. 2008, *MNRAS*, 390, 693
- Drukier, G. A., Cohn, H. N., Lugger, P. M., Slavin, S. D., Berrington, R. C., & Murphy, B. W. 2007, *AJ*, 133, 1041
- Dupree, A. K. 1986, *ARA&A*, 24, 377
- Dupree, A. K., Hartmann, L., & Avrett, E. H. 1984, *ApJ*, 281, L37
- Dupree, A. K., Sasselov, D. D., & Lester, J. B. 1992, *ApJ*, 387, L85
- Ferraro, F. R., Paltrinieri, B., Fusi Pecci, F., Cacciari, C., Dorman, B., & Rood, R. T. 1997, *ApJ*, 484, L145
- Harris, W. E. 1996, *AJ*, 112, 1487
- Helling, C., Winters, J. M., & Sedlmayr, E. 2000, *A&A*, 358, 651
- Johnson, C. I., Kraft, R. P., Pilachowski, C. A., Sneden, C., Ivans, I. I., & Benman, G. 2005, *PASP*, 117, 1308
- Kadla, Z. I. 1966, *Izv. Glav. Astron. Obs.*, 181, 93
- Kemp, S. N., & Bates, B. 1995, *A&AS*, 112, 513
- Kopacki, G. 2001, *A&A*, 369, 862
- Kopacki, G., Kołaczkowski, Z., & Pigulski, A. 2003, *A&A*, 398, 541
- Lee, J. W., & Carney, B. W. 1999, *AJ*, 118, 1373
- Lee, Y-W., Demarque, P., & Zinn, R. 1994, *ApJ*, 423, 248
- Lee, Y-W., et al. 2005, *ApJ*, 621, L57
- Ludendorff, H. 1905, *Publikationen des Astrophysikalischen Observatoriums zu Potsdam*, 50
- Lupton, R. H., Gunn, J. E., & Griffin, R. F. 1987, *AJ*, 93, 1114
- Marshall, J. R., vanLoon, J. Th., Matsuura, M., Wood, P. R., Zijlstra, A. A. & Whitelock, P. A. 2004, *MNRAS*, 355, 1348
- Mauas, P. J. D., Cacciari, C., & Pasquini, L. 2006, *A&A*, 454, 615
- Mayor, M. et al. 1984, *A&A*, 134, 118
- McDonald, I., & van Loon, J. T. 2007, *A&A*, 476, 1261

- McDonald I., van Loon, J. T., Decin, L., Boyer, M. L., Dupree, A. K., Evans A., Gehrz, R. D., & Woodward, C. E. 2009, MNRAS, in press (arXiv:0812.0326)
- Mészáros, Sz., Dupree, A. K., & Szentgyorgyi, A. H. 2008, AJ, 135, 1117
- Nardetto, N., Mourard, D., Kervella, P., Mathias, P., Mérand, A., & Bersier, D. 2006, A&A, 453, 309
- Peterson, R. C., Rood, R. T., & Crocker, D. A. 1995, ApJ, 453, 214
- Petterson, O. K. L., Cottrell, P. L., Albrow, M. D., & Fokin, A. 2005, MNRAS, 362, 1167
- Pilachowski, C. A., Sneden, C., Kraft, R. P., & Langer, G. E. 1996, AJ, 112, 545
- Piotto, G., Bedin, L. R., Anderson, J., King, I. R., Cassisi, S., Milone, A. P., Villanova, S., Pietrinferni, A., & Renzini, A. 2007, ApJ, 661, L53
- Recio-Blanco, A., Aparicio, A., Piotto, G., de Angeli, F., & Djorgovski, S. G. 2006, A&A, 452, 875
- Renzini, A. 1981, in Phys. Proc. in Red Giants, I. Iben & A. Renzini, eds. (Dordrecht: Reidel), 431
- Russeva, T., & Russev, R. 1980, IBVS, 1769
- Sandage, A. 1970, ApJ, 162, 841
- Sandage, A., & Walker, M. F. 1966, ApJ, 143, 313
- Sandage, A., & Wallerstein, G. 1960, ApJ, 131, 598
- Sandage, A., & Wildey, R. 1967, ApJ, 150, 469
- Sarajedini, A. 1997, AJ, 113, 682
- Sarajedini, A., Chaboyer, B., & Demarque, P. 1997, PASP, 109, 1321
- Searle, L., & Zinn, R. 1978, ApJ, 225, 357
- Shetrone, M. D. 1994, PASP, 106, 161
- Sills, A., & Pinsonneault, M. H. 2000, ApJ, 540, 489
- Skrutskie, M.F. et al. 2006, AJ, 131, 1163
- Smith, G. H., Dupree, A. K., & Strader, J. 2004, PASP, 116, 819
- Sneden, C., Pilachowski, C. A., & Kraft, R. P. 2000, AJ, 120, 1351
- Soderberg, A. M., Pilachowski, C. A., Barden, S. C., Willmarth, D., & Sneden, C. 1999, PASP, 111, 1233

- Soker, N., Rappaport, S., & Fregeau, J. 2001, *ApJ*, 563, L87
- Stetson, P. B., Vandenberg, D. A., & Bolte, M. 1996, *PASP*, 108, 560
- Sweigart, A. V. 1997, *ApJ*, 474, L23
- Szentgyorgyi, A. H., Cheimets, P., Eng, R., Fabricant, D. G., Geary, J. C., Hartmann, L., Pieri, M. R., & Roll, J. B. 1998, in *Proc. SPIE Vol. 3355, Optical Astronomical Instrumentation*, ed. Sandro D'Odorico, 242
- Vandenberg, D. A., Bolte, M., & Stetson, P. B. 1990, *AJ*, 100, 445
- Wachter, A., Schröder, K.-P., Winters, J. M., Arndt, T. U., & Sedlmayr, E. 2002, *A&A*, 384, 452
- Wachter, A., Winters, J. M., Schröder, K.-P., & Sedlmayr, E. 2008, *A&A*, 486, 497
- Zarro, D. M., & Rodgers, A. W. 1983, *A&AS*, 53, 815

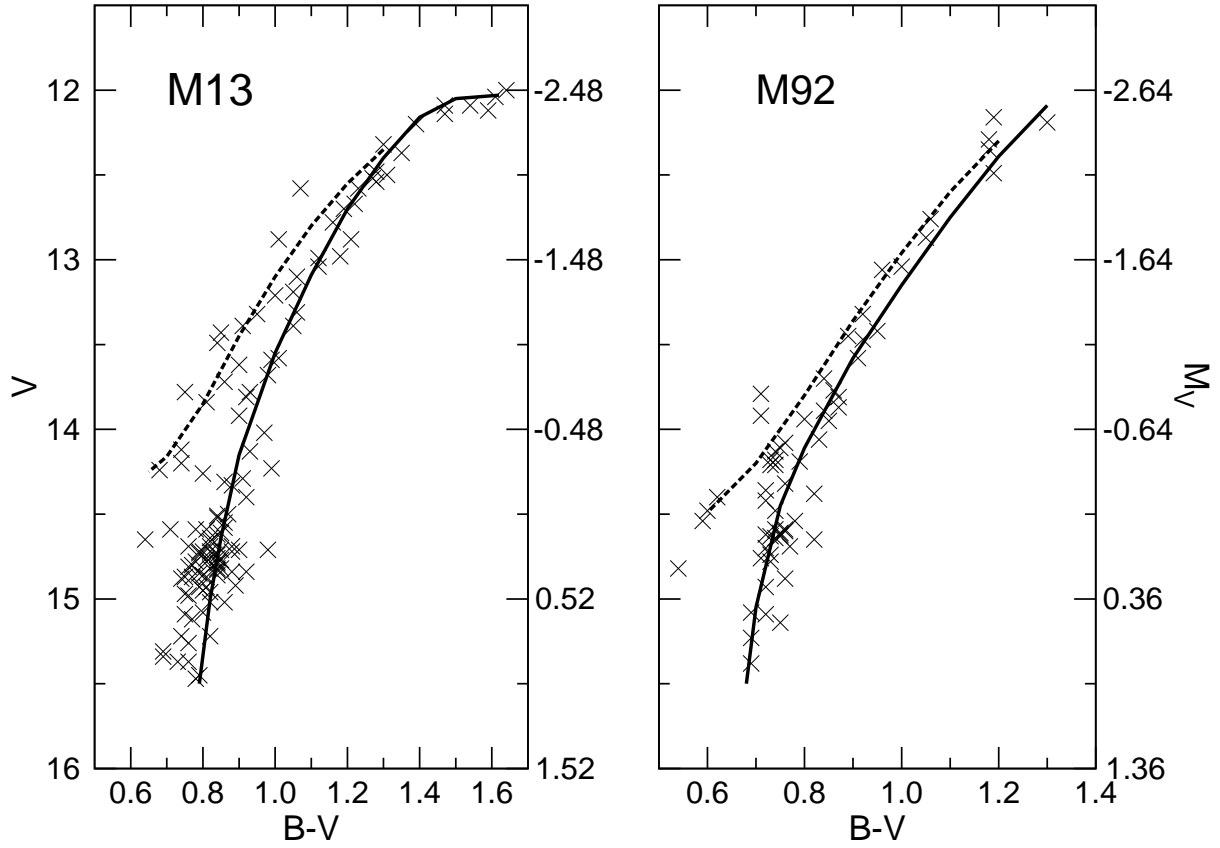


Fig. 1.— Color-magnitude diagram for all stars observed in M13 and M92. The solid line shows the fiducial curve of the RGB; the dashed line shows the fiducial curve of the AGB for both clusters taken from observations of Sandage (1970). The absolute magnitudes were calculated using the apparent distance modulus  $(m - M)_V = 14.48$  for M13 and  $(m - M)_V = 14.64$  for M92 from Harris (1996).

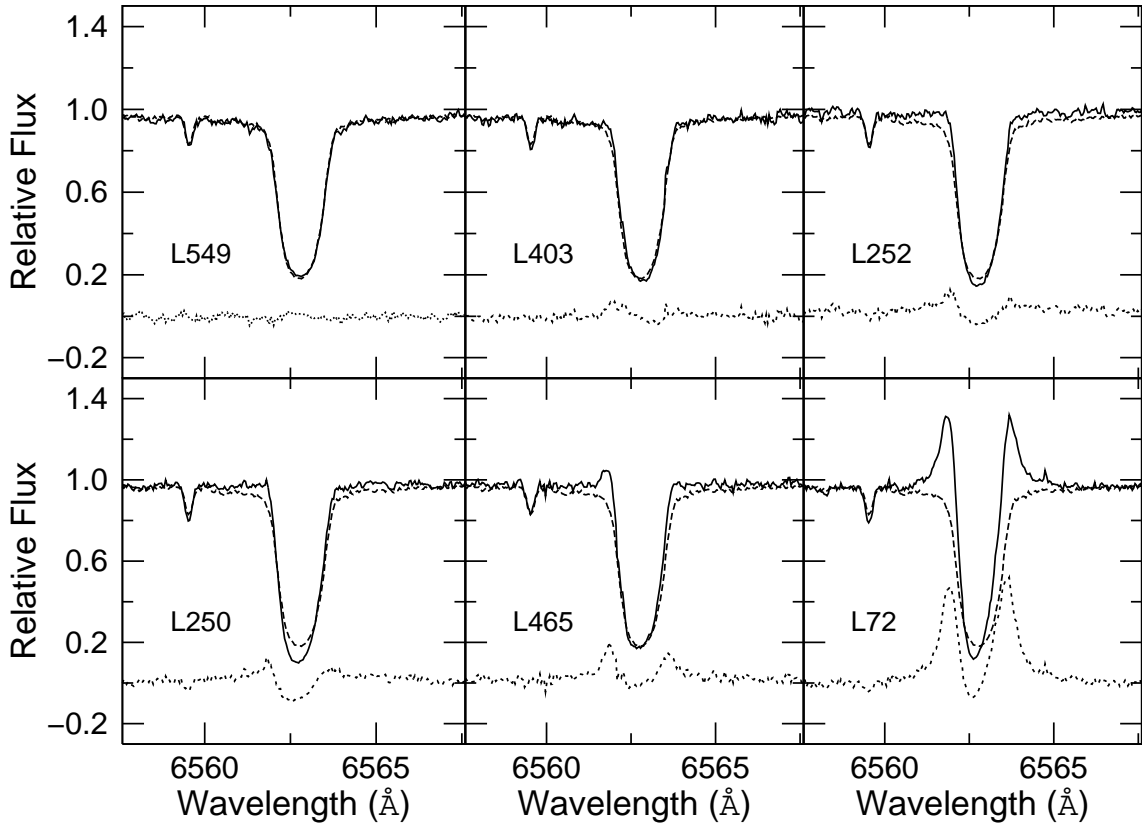


Fig. 2.— Examples of the effect of subtracting an averaged spectrum (dashed line) from the observed spectra (solid lines) for stars in M13. The difference spectrum is shown by a dotted line below. L549 is a star without any emission; the error of the subtracted spectrum (dotted line) is smaller than 0.02 of the continuum level. In the case of L403, weak emission on the short wavelength is visible, however it is comparable to the noise of the observed spectrum and extends to the core of the line, so it was not identified as emission. L252 is an example of how the continuum normalization can shift the region near  $H\alpha$  making it hard to identify the emission. The blue emission in the spectrum of L250 might be missed by eye, but the subtraction method clearly shows the presence of emission. L465 and L72 are examples of emission that is clearly visible in the spectrum above the continuum level.

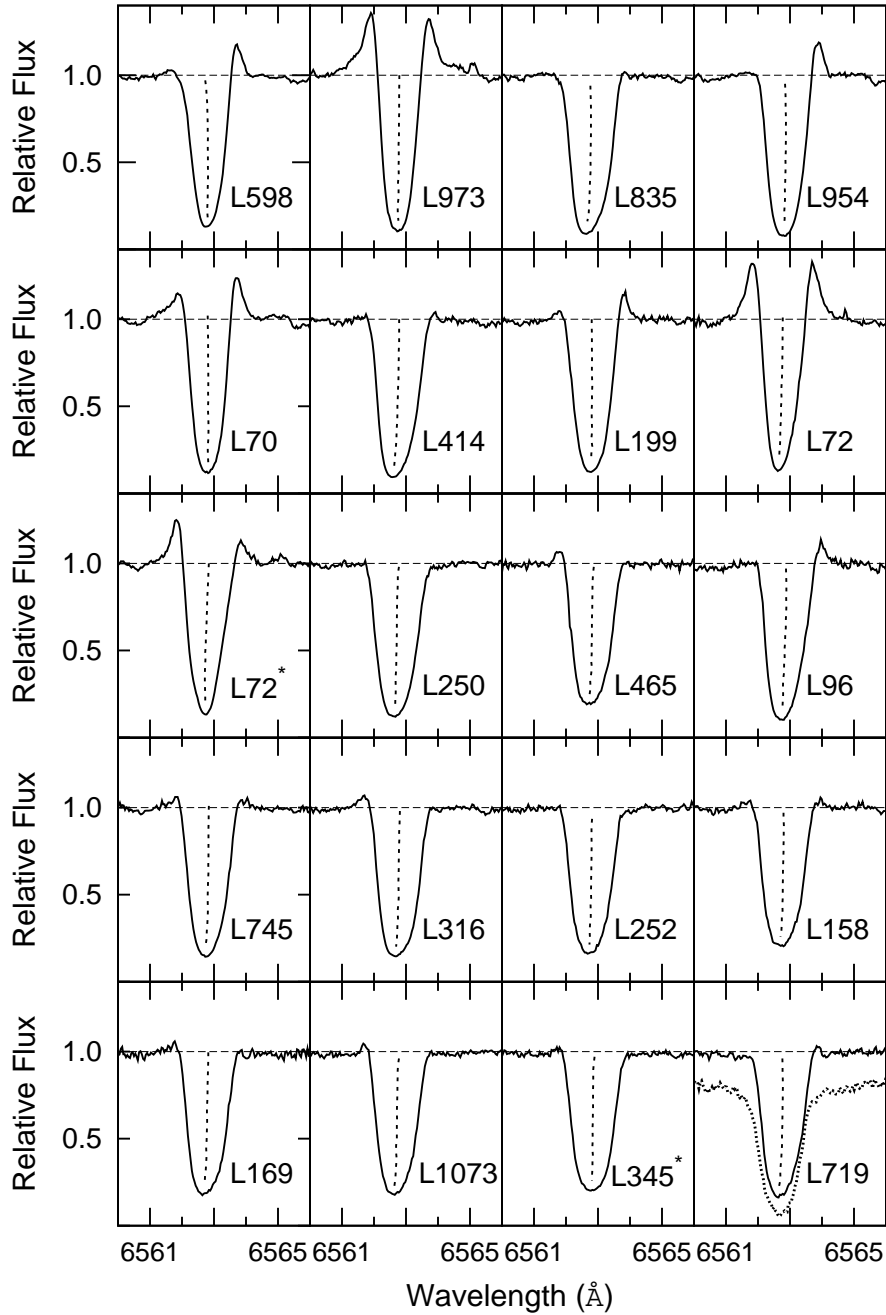


Fig. 3.— Normalized spectra of red giants in M13 which showed emission in  $H\alpha$  on 2006 March 14. Stars marked with \* were observed on 2006 May 10. The dashed line marks the bisector. The emission of one star, L719, disappeared between observations, and the spectrum is overlaid here using a dotted line. The spectra are arranged in order of decreasing brightness; the brightest is at the top left and the stars become fainter from left to right. The wavelength scale is corrected for heliocentric velocity. The radial velocity of M13 is  $-243.5 \pm 0.2 \text{ km s}^{-1}$ .

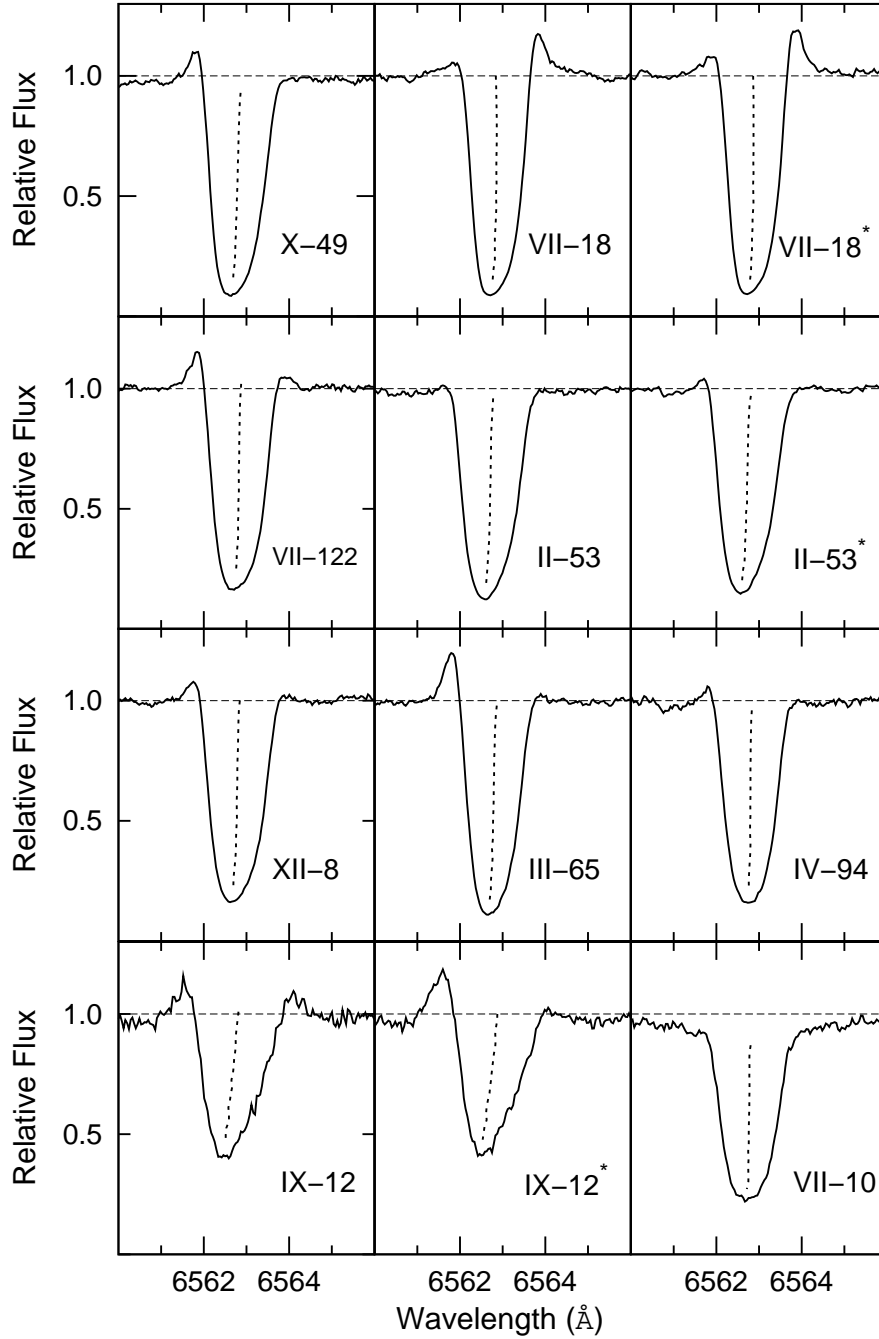


Fig. 4.— Normalized spectra of red giants in M92 which showed emission in H $\alpha$  on 2006 May 7. Stars marked with \* were observed on 2006 May 9. VII-10 is an example of an H $\alpha$  profile without emission. For explanation please see Figure 3 caption. The radial velocity of M92 is  $-118.0 \pm 0.2 \text{ km s}^{-1}$ .

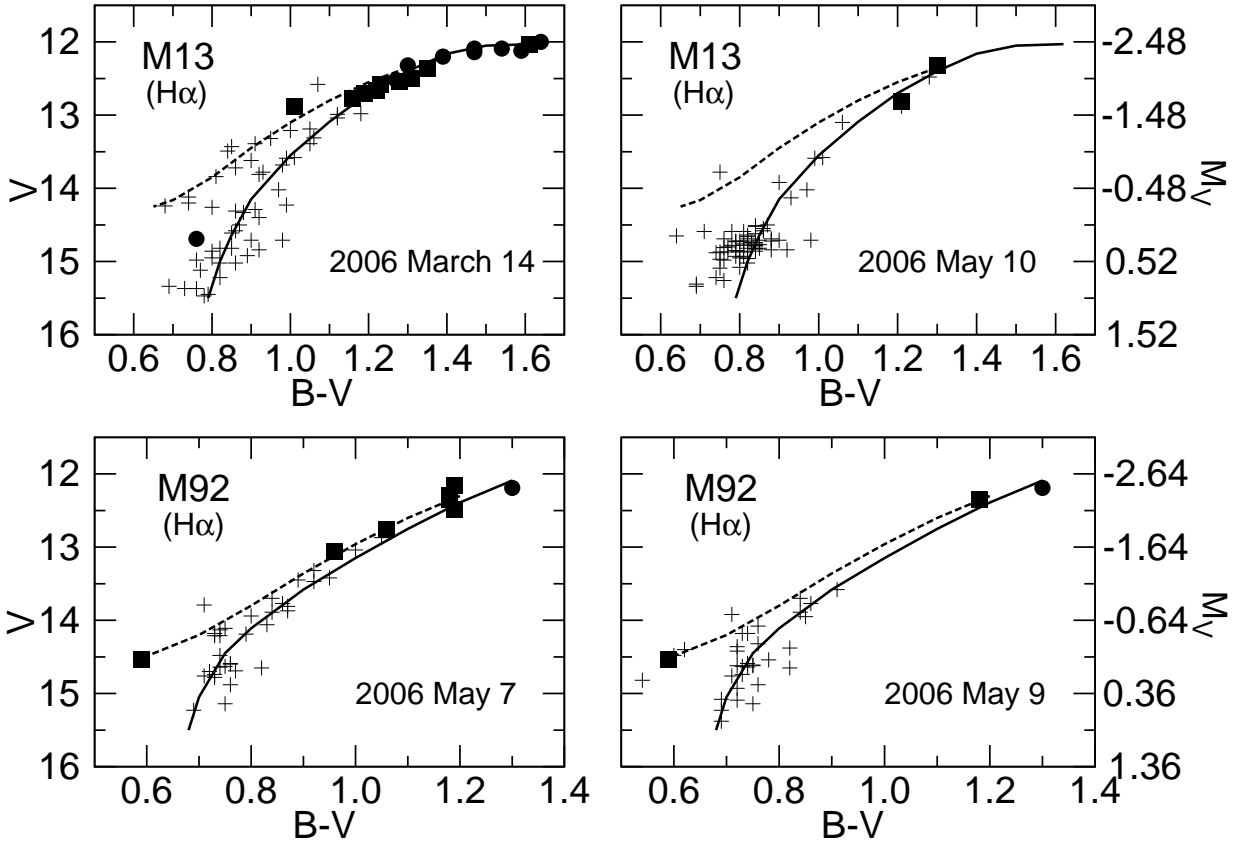


Fig. 5.— Color-magnitude diagrams for all M13 and M92 stars observed in 2006. Stars with  $H\alpha$  emission and with  $B < R$  (indicating outflow) are marked with filled circles; stars with  $B > R$  emission wings (suggests inflow) are denoted by filled squares. The solid line shows the fiducial curve of the RGB; dashed lines show the fiducial curve of the AGB for M13 and M92 from observations of Sandage (1970).



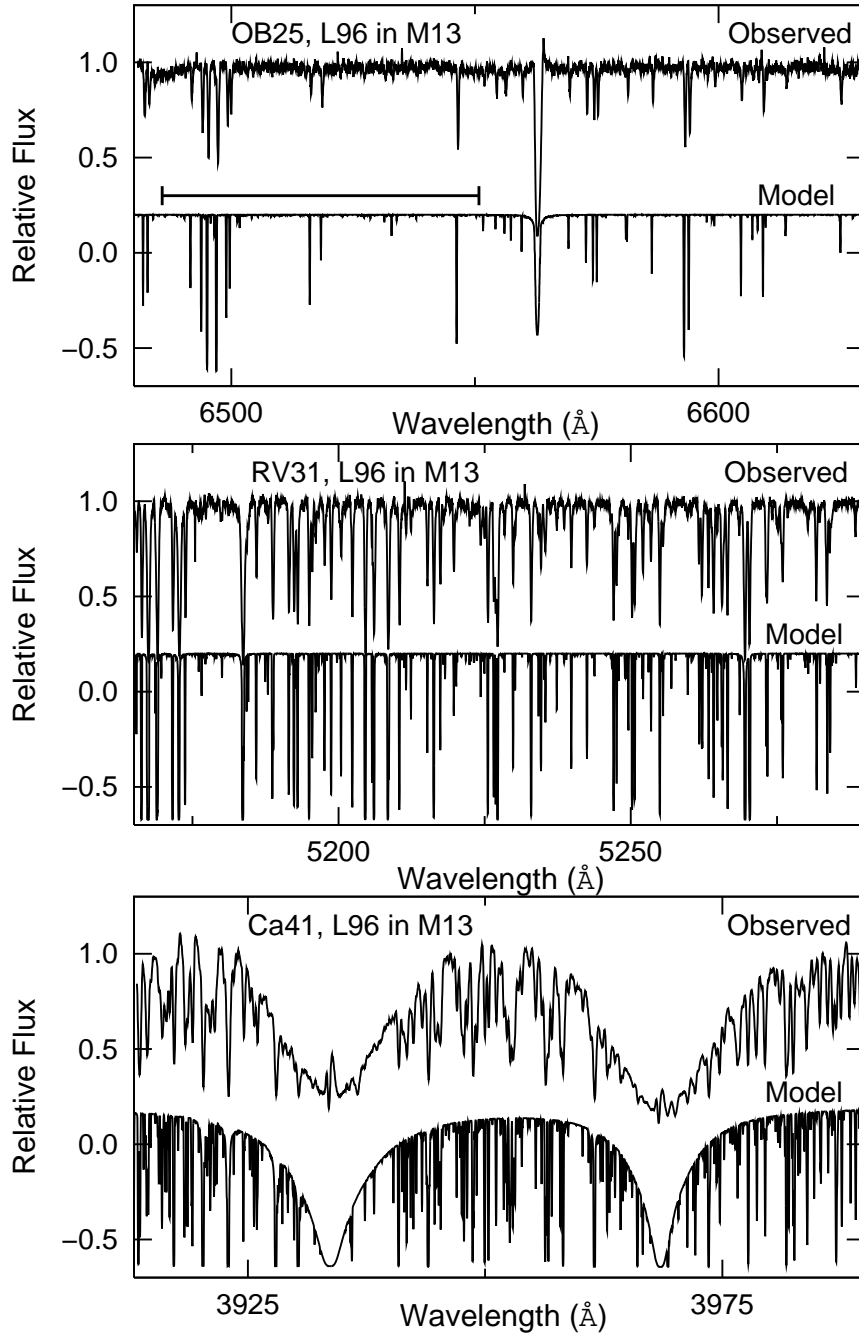


Fig. 6.— Continuum normalized spectra of a sample star (L96) in M13 showing  $H\alpha$ , RV31, and Ca II H&K spectra after all reductions. Upper spectrum is the observed one, lower spectrum is the model synthesis of a star (Coelho et al. 2005, using Kurucz models) with the highest amplitude of the cross-correlation function from the  $H\alpha$  region. The cross-correlation region used in the OB25 filter is marked in the spectrum and chosen to avoid  $H\alpha$ .

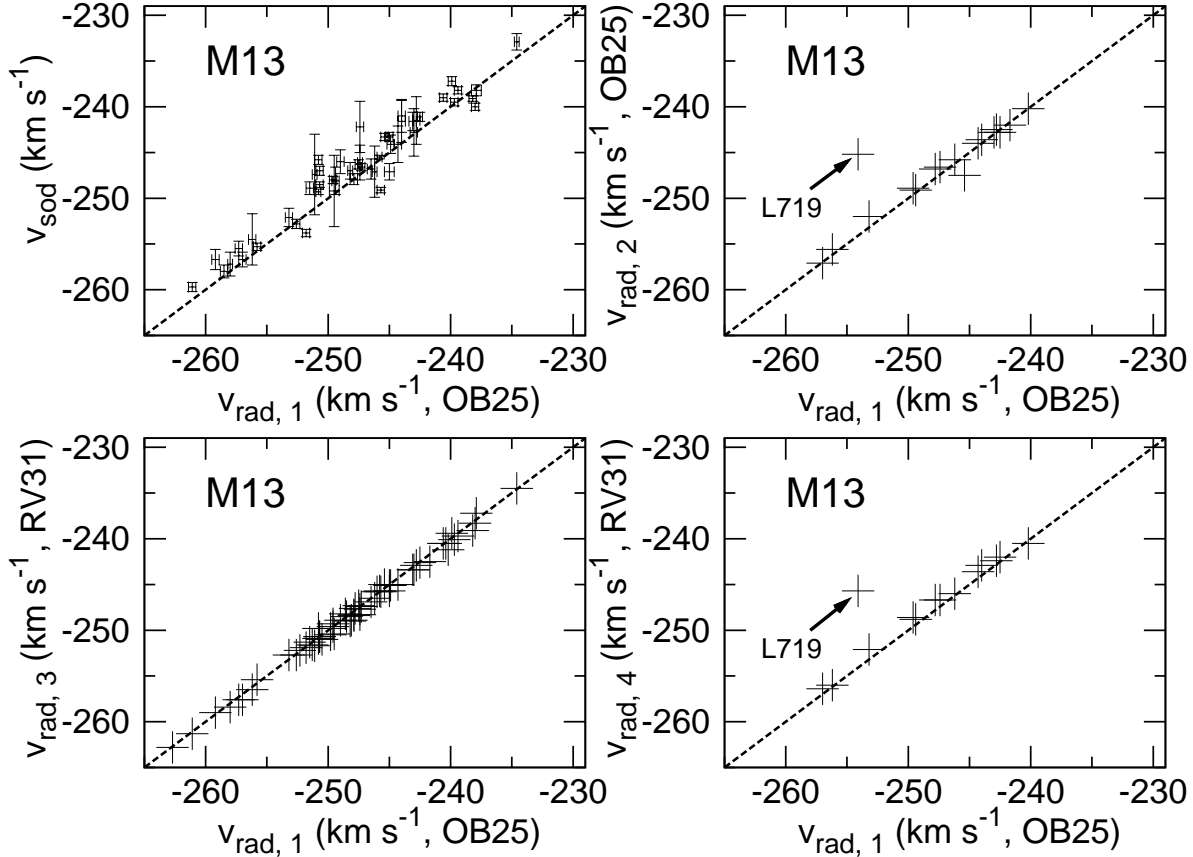


Fig. 7.— Top left: Radial velocities measured with the  $H\alpha$  filter (OB25) in this paper on 2006 March 14 ( $v_{rad,1}$ ) compared to the same stars observed by Soderberg et al. (1999) ( $v_{sod}$ ). There is a slight offset ( $1.1 \pm 0.5 \text{ km s}^{-1}$ ) between all observations taken in 2006 and observations for the same stars from Soderberg et al. (1999). Top right: Radial velocities measured in this paper on 2006 March 14 ( $v_{rad,1}$ ) for the same stars observed on 2006 May 10 with the  $H\alpha$  filter ( $v_{rad,2}$ ). Lower left: Radial velocity measured with Hectochelle for the same stars observed on 2006 March 14 ( $v_{rad,1}$ ) compared to the observations with the RV31 filter on 2006 March 16 ( $v_{rad,3}$ ). Lower right: Radial velocities for the same stars measured with Hectochelle on 2006 March 14 ( $v_{rad,1}$ ) compared to the observations with the RV31 filter on 2006 May 10 ( $v_{rad,4}$ ). The dashed line marks a 1:1 relation in all panels. The error of our measurements was generally smaller than the symbols used in the figure. The anomalous star in M13, L719, lies between the AGB and RGB, and the large velocity change may indicate binarity.

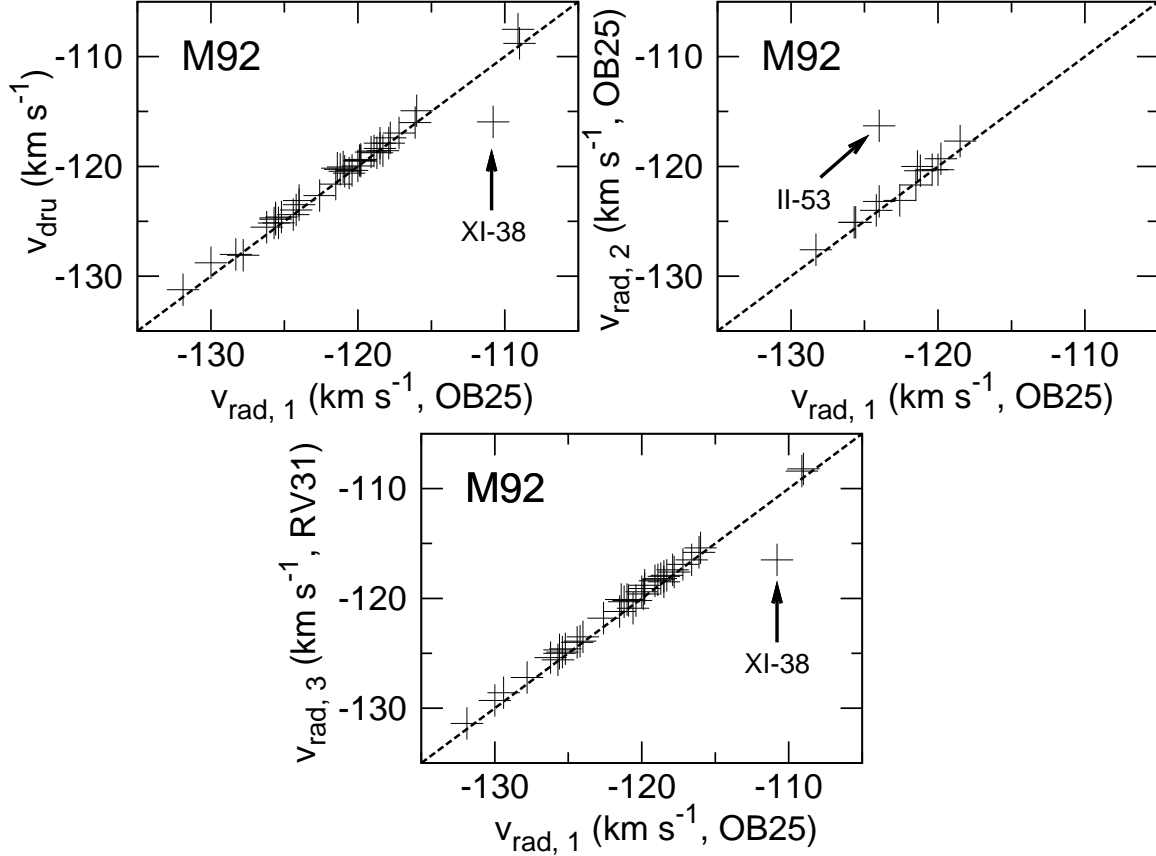


Fig. 8.— Top left: Radial velocities measured with the H $\alpha$  filter in this paper on 2006 May 7 ( $v_{rad,1}$ ) compared to the same stars observed by Drukier et al. (2007) ( $v_{dru}$ ). Top right: Radial velocities measured in this paper on 2006 May 7 ( $v_{rad,1}$ ) for the same stars observed on 2006 May 9 with the H $\alpha$  filter ( $v_{rad,2}$ ). Center: Radial velocity measured with Hectochelle for the same stars observed on 2006 May 7 ( $v_{rad,1}$ ) compared to the observations with the RV31 filter on the same day ( $v_{rad,3}$ ). There is no offset larger than the error of measurements between any observations. The dashed line marks a 1:1 relation in all panels. There is good agreement between all observations taken in May and observations for the same stars from Drukier et al. (2007). The error of our measurements was generally smaller than the symbol we used in the figure. For discussion of the two outlier stars see Section 4.1.

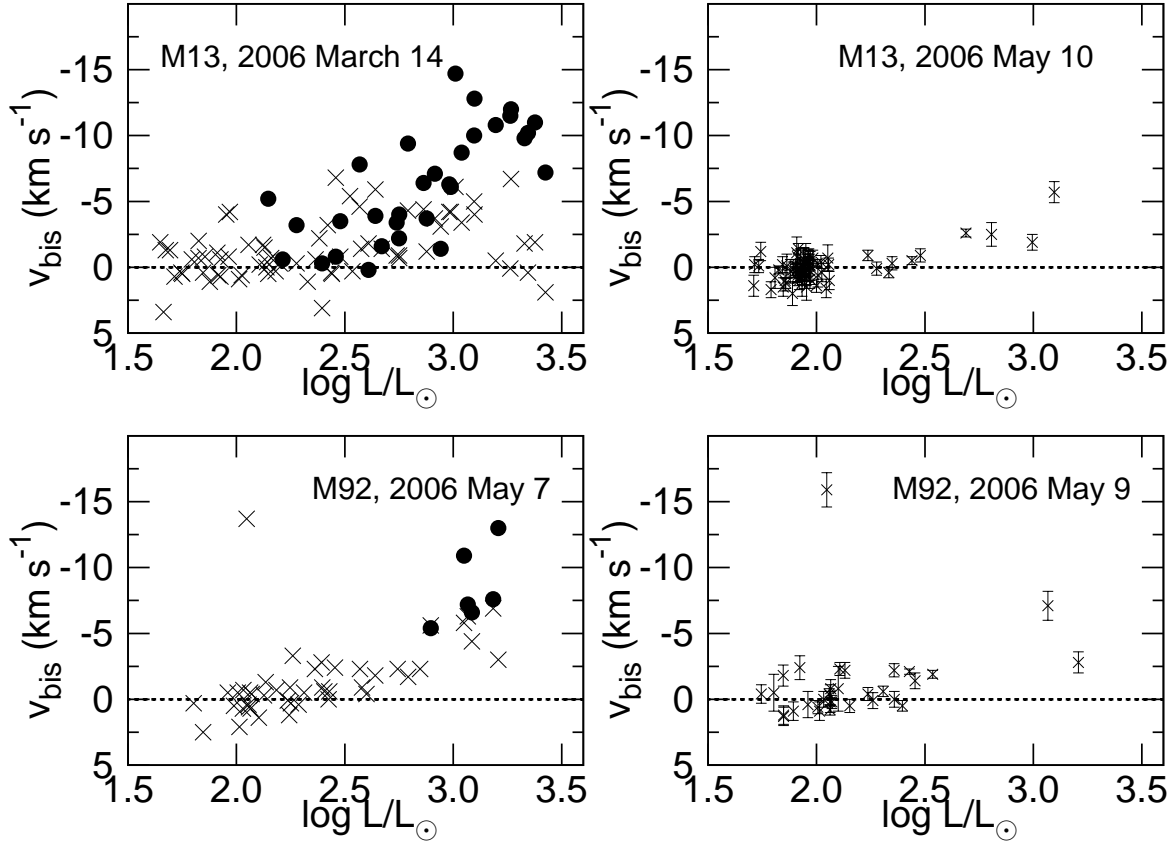


Fig. 9.— The velocity difference ( $v_{bis}$ ) between the top and the bottom of the bisector of  $H\alpha$  ( $\times$ ) and the coreshift of the Ca II K central reversal absorption (filled circle) as a function of luminosity. All Ca observations from different days are plotted together on the left side panels. Negative values indicate a blueshifted core (outward motion), positive values denote a red shifted core (inward motion). The error bars in figures on the left side were eliminated to display the differences between  $H\alpha$  and Ca II K. A predominant outward motion sets in near  $\log L/L_{\odot} \approx 2.5$  in both clusters and increases in velocity towards higher luminosity. The velocity of the Ca II K central reversal formed higher in the chromosphere than the  $H\alpha$  core, is generally larger than the bisector velocity of  $H\alpha$  at the same luminosity, indicating that the expansion velocity increases with height in the chromosphere.

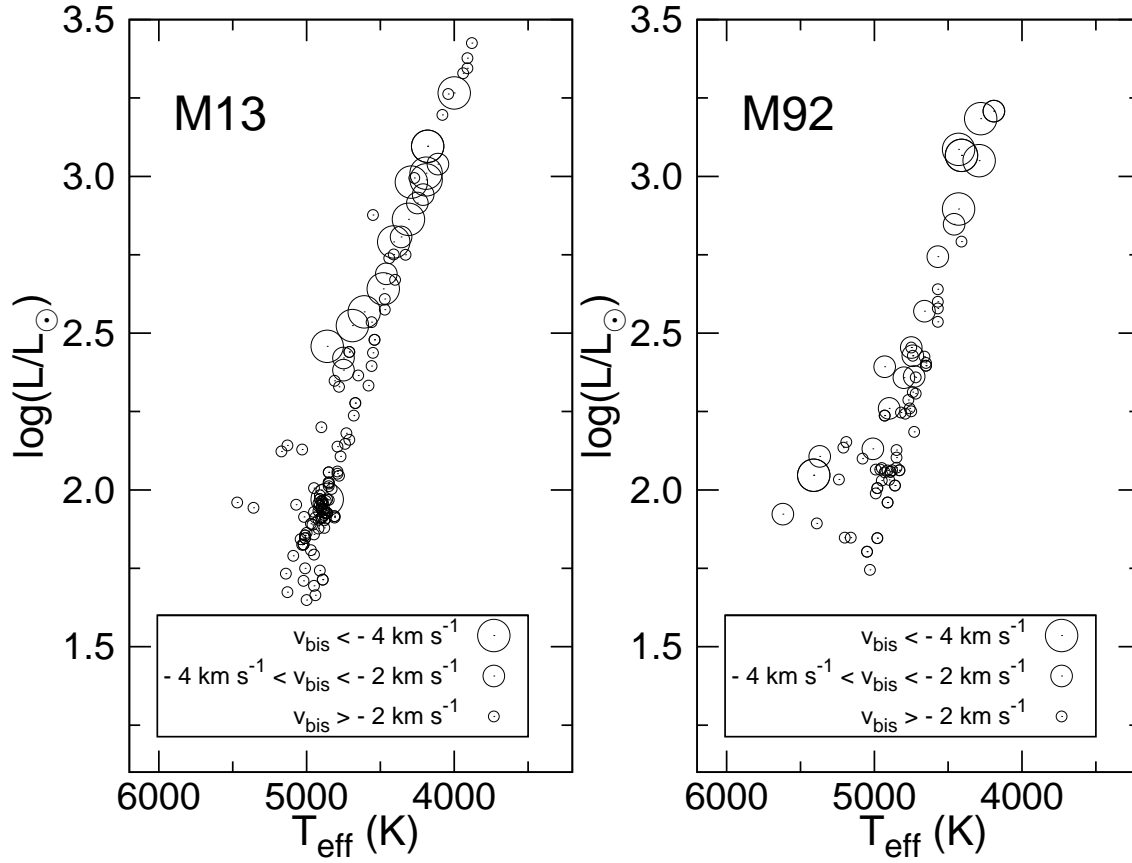


Fig. 10.— Temperature-luminosity diagram for all stars observed in both clusters, where the size of the circle indicates the velocity of the  $H\alpha$  bisector asymmetry. Big circle:  $v_{bis} < -4 \text{ km s}^{-1}$ , medium circle:  $-4 \text{ km s}^{-1} < v_{bis} < -2 \text{ km s}^{-1}$ , small circle:  $v_{bis} > -2 \text{ km s}^{-1}$ . Concentric circles indicate multiple observations of the same star.

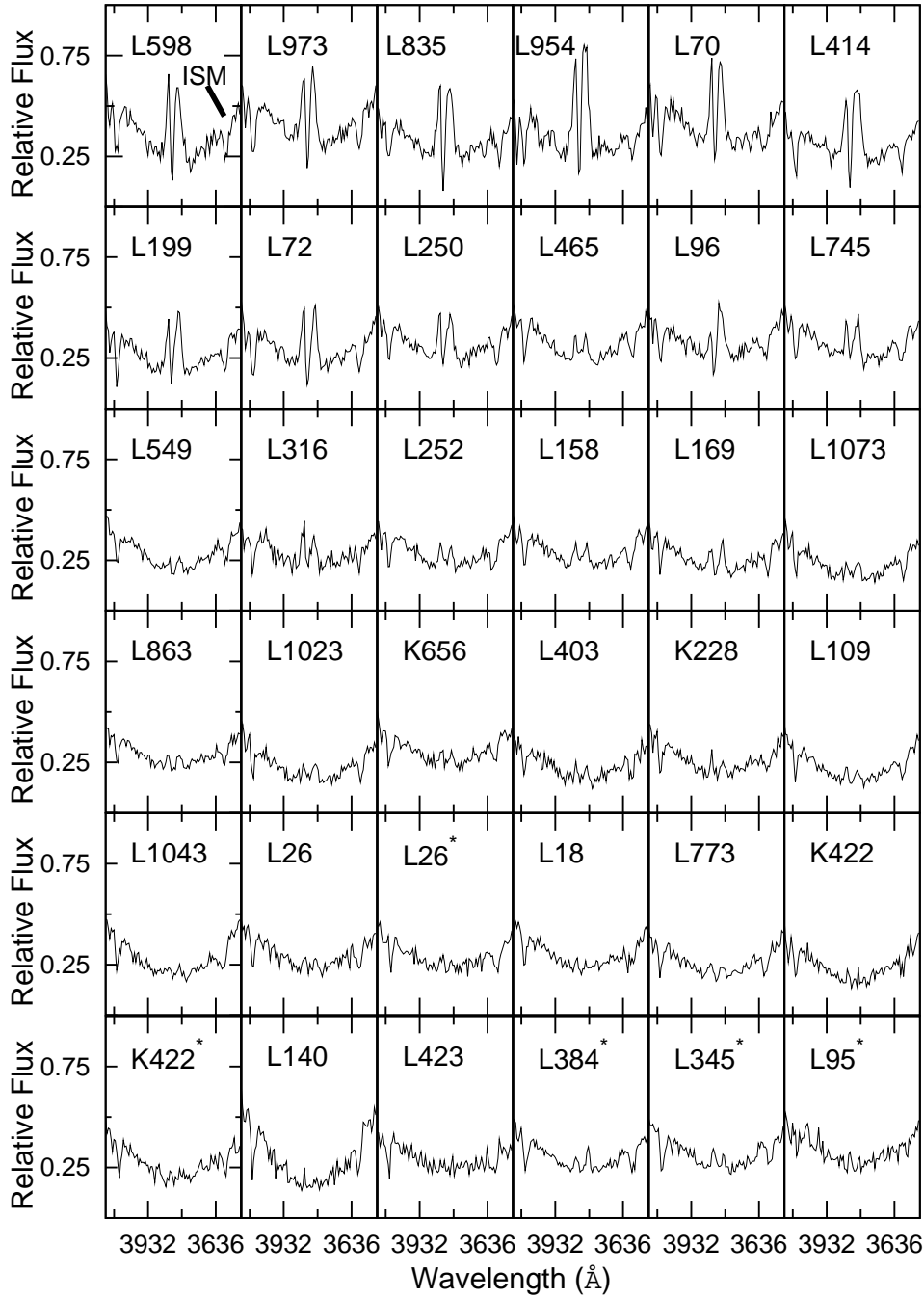


Fig. 11.— Spectra of the brightest red giants in M13 which showed emission in Ca II K on 2006 March 14. The spectra are smoothed by 3. The spectra are arranged in order of decreasing brightness; the brightest is at the top left and the stars become fainter from left to right for a single date. The object names marked by stars were observed on 2006 May 10. The wavelength scale is corrected for heliocentric velocity. The line marked ISM in the spectrum of L598 denotes absorption by the interstellar medium and can be recognized in the other spectra.

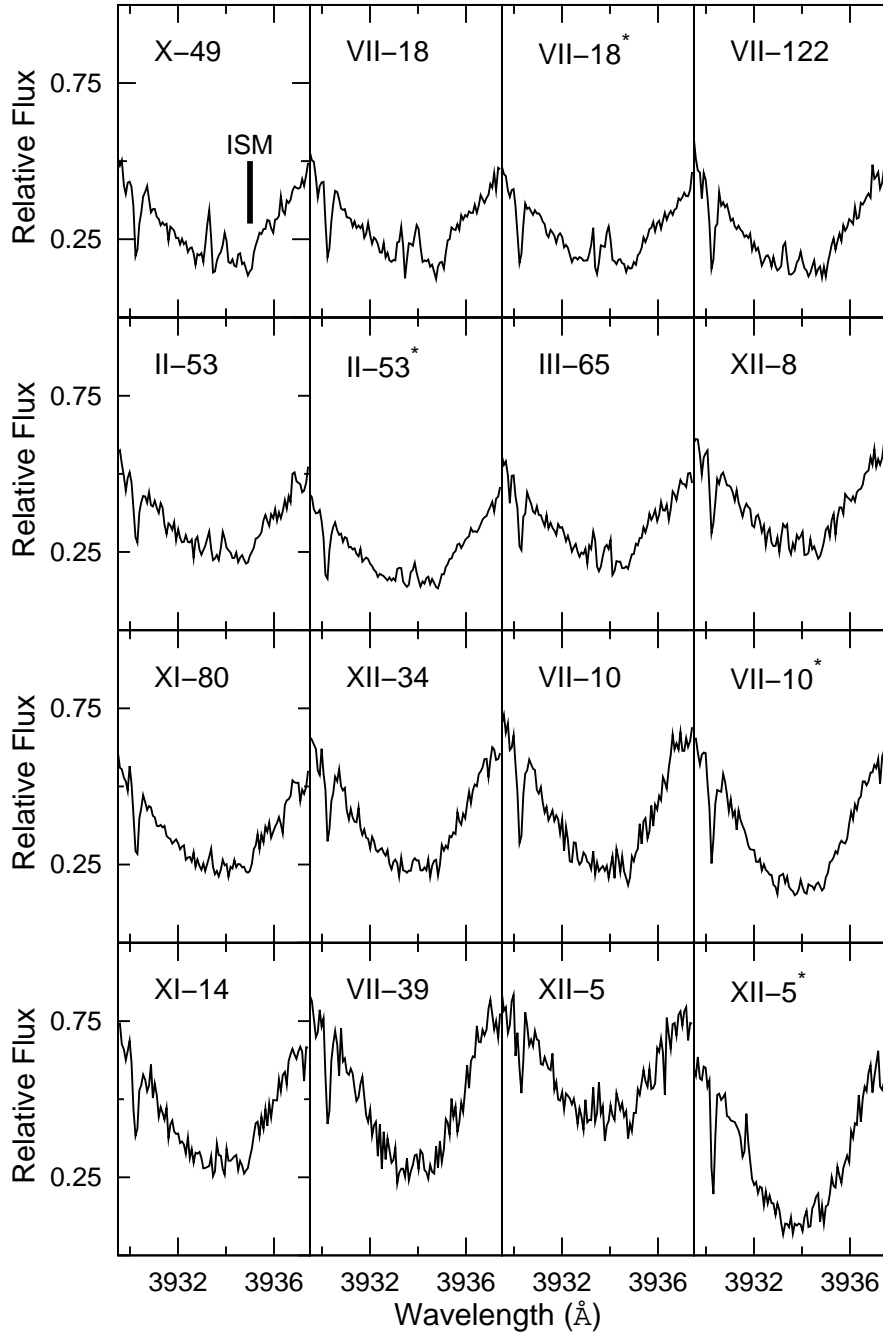


Fig. 12.— Spectra of the brightest red giants in M92 which showed emission in Ca II K on 2006 May 7. The object names marked by stars were observed on 2006 May 9. Observations obtained on 2006 May 7 have generally lower S/N due to bad sky conditions and resulted in a higher Ca II K core of XII-5, the faintest star in our sample. Additional explanation can be found in the caption of Figure 11.

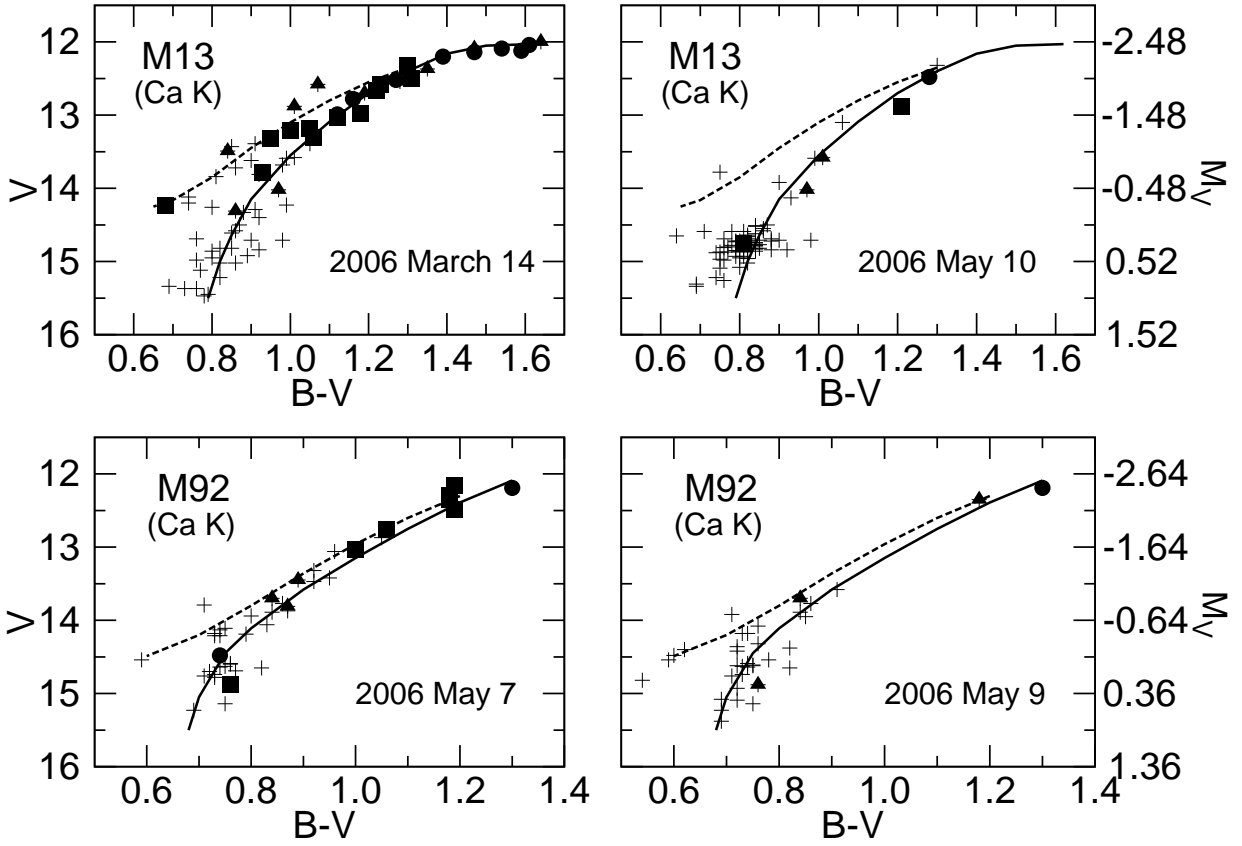


Fig. 13.— Color-magnitude diagrams for all M13 and M92 stars observed. Stars with Ca II K emission and with  $B < R$  (indicating outflow) are marked with circles; stars with  $B > R$  emission wings (suggests inflow) are denoted by squares and stars with  $B \approx R$  are marked with triangles. The solid line shows the fiducial curve of the RGB; dashed lines show the fiducial curve of the AGB for M13 and M92 from observations of Sandage (1970).



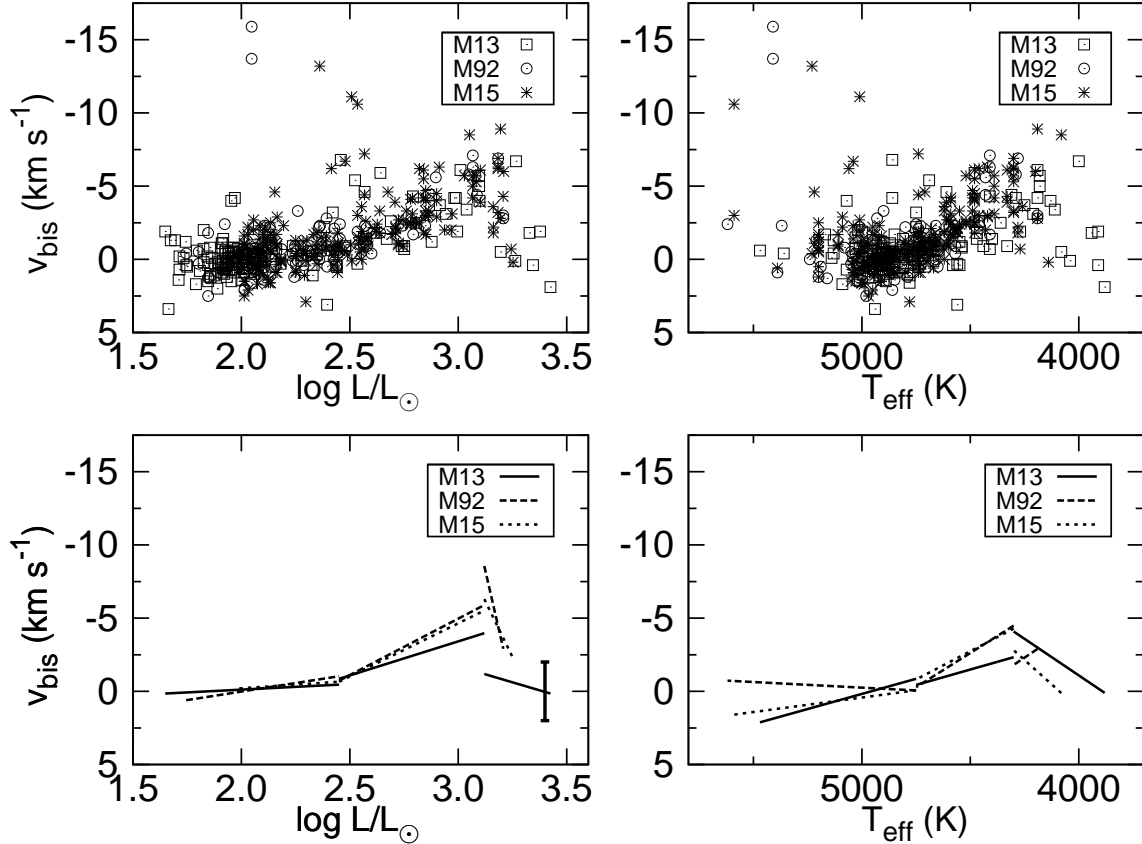


Fig. 14.— *Top left and right:* The bisector velocity ( $v_{bis}$ ) of  $H\alpha$  for all observations in M13, M15 and M92 as a function of luminosity and effective temperature. Negative values indicate outflow. *Lower left and right:* To fit the results with a linear function, luminosity and effective temperature were divided into three different regions: the bottom of the RGB [ $\log(L/L_{\odot}) = 1.6 - 2.5$ ,  $T_{eff}=4750-5700$  K], where  $v_{bis}$  was close to zero  $\text{km s}^{-1}$ ; the RGB stars [ $\log(L/L_{\odot}) = 2.5 - 3.1$ ,  $T_{eff}=4300-4750$  K], where  $v_{bis}$  shows a significant increase; and the top of the RGB [ $\log(L/L_{\odot}) = 3.1 - 3.5$ ,  $T_{eff}=3800-4300$  K], where  $v_{bis}$  generally shows smaller values than in the middle of the RGB. The stars with high velocity near  $\log(L/L_{\odot}) = 2.2 - 2.4$  were omitted from the fit. Error bar of the top of the RGB fit for M13 is displayed in the lower left panel (for details see Section 6.3). The errors of the fits span between  $\sim 1$  and  $2.5$   $\text{km s}^{-1}$  for each fit.

Table 1. Photometric Data of Observed Cluster Members in M13

ID No. <sup>a</sup>	RA(2000) <sup>b</sup>	Dec(2000) <sup>b</sup>	B	V	J	H	K	B–V	V–K	Obs. <sup>c</sup>
III-65 <sup>d</sup>	16 41 39.091	+36 23 51.40	16.04	15.22	13.690	13.220	13.071	0.82	2.15	1,3,5
K188 <sup>e</sup>	16 40 42.982	+36 27 41.88	14.44	13.39	11.410	10.784	10.704	1.05	2.69	1,3,5
K210 <sup>e</sup>	16 40 56.378	+36 22 18.51	15.21	14.33	12.580	12.028	11.966	0.88	2.36	1,3,5
K220 <sup>e</sup>	16 41 02.608	+36 26 15.81	15.74	14.98	13.353	12.899	12.833	0.76	2.15	1,2,4,5,6
K223 <sup>e</sup>	16 41 05.075	+36 28 20.85	15.56	14.71	13.093	12.565	12.494	0.85	2.22	2,4,6

<sup>a</sup>Ludendorff (1905) is the identification for the majority of the stars denoted by L.

<sup>b</sup>2MASS coordinates (Skrutskie et al. 2006)

<sup>c</sup>Observations: 1: 2006 March 14 (OB25), 2: 2006 May 10 (OB25), 3: 2006 March 16 (RV31), 4: 2006 May 10 (RV31), 5: 2006 March 16 (Ca41), 6: 2006 May 10 (Ca41).

<sup>d</sup>Arp (1955)

<sup>e</sup>Kadla (1966)

Note. — The visual photometry is taken from Cudworth & Monet (1979), J,H,K photometry is taken from the 2MASS Catalog (Skrutskie et al. 2006). This table is available in its entirety in a machine-readable form in the on-line journal. A portion is shown here for guidance regarding its form and content.

Table 2. Photometric Data of Observed Cluster Members in M92

ID No. <sup>a</sup>	RA(2000) <sup>b</sup>	Dec(2000) <sup>b</sup>	B	V	J	H	K	B–V	V–K	Obs. <sup>c</sup>
I-14	17 17 28.77	43 10 02.8	15.47	14.74	13.155	12.644	12.592	0.73	2.148	1,2,3,4,5
I-40	17 17 22.68	43 08 50.5	15.51	14.78	13.258	12.777	12.640	0.73	2.140	1,3,4
I-67	17 17 21.24	43 08 27.0	14.24	13.32	11.406	10.870	10.766	0.92	2.554	1,3,4
I-68	17 17 21.73	43 08 15.8	15.36	14.61	13.243	12.825	12.661	0.75	1.949	2,5
II-6	17 17 50.37	43 13 46.0	15.89	15.14	13.541	13.002	12.992	0.75	2.148	1,2,3,4,5

<sup>a</sup>Sandage & Walker (1966)

<sup>b</sup>2MASS coordinates (Skrutskie et al. 2006)

<sup>c</sup>Observations: 1: 2006 May 7 (OB25), 2: 2006 May 9 (OB25), 3: 2006 May 7 (RV31), 4: 2006 May 8 (Ca41), 5: 2006 May 9 (Ca41).

Note. — The visual photometry is taken from Cudworth (1976), J,H,K photometry is taken from the 2MASS Catalog (Skrutskie et al. 2006). This table is available in its entirety in a machine-readable form in the on-line journal. A portion is shown here for guidance regarding its form and content.

Table 3. Hectochelle Observations of M13 and M92

Date (UT)	Total exp. (s)	Wavelength (Å)	Filter Name	Number of Observed Stars
2006 March 14 (M13, Field 1)	3 × 2400	6475–6630	OB25	70
2006 March 16 (M13, Field 1)	3 × 2400	3910–3990	Ca41	70
2006 March 16 (M13, Field 1)	1 × 2400	5150–5300	RV31	65
2006 May 10 (M13, Field 2)	3 × 2400	6475–6630	OB25	70
2006 May 10 (M13, Field 2)	3 × 2400	3910–3990	Ca41	63
2006 May 10 (M13, Field 2)	1 × 2400	5150–5300	RV31	65
2006 May 7 (M92, Field 1)	3 × 2400	6475–6630	OB25	42
2006 May 7 (M92, Field 1)	3 × 1800	5150–5300	RV31	40
2006 May 8 (M92, Field 1)	3 × 2400	3910–3990	Ca41	41
2006 May 9 (M92, Field 2)	3 × 1800	6475–6630	OB25	36
2006 May 9 (M92, Field 2)	3 × 2400	3910–3990	Ca41	36

Table 4. B/R ratio of H $\alpha$  Line for Stars with Emission Wings

ID No.	M13		ID No.	M92	
	<i>B/R</i>	<i>B/R</i>		<i>B/R</i>	<i>B/R</i>
	2006 March 14	2006 May 10		2006 May 7	2006 May 9
L70	< 1	...	II-53	> 1	> 1
L72	< 1	> 1	III-65	> 1	...
L96	< 1	...	IV-94	> 1	...
L158	> 1	...	VII-18	< 1	< 1
L169	> 1	...	VII-122	> 1	...
L199	< 1	...	IX-12	> 1	> 1
L250	> 1	...	X-49	> 1	...
L252	> 1	...	XII-8	> 1	...
L316	> 1	...			
L345	...	> 1			
L414	< 1	...			
L465	> 1	...			
L598	< 1	...			
L719	< 1	no emission			
L745	> 1	...			
L835	< 1	...			
L954	< 1	...			
L973	> 1	...			
L1073	> 1	...			

Note. — The parameter B/R is the intensity ratio of Blue (short wavelength) and Red (long wavelength) emission peaks. The symbol ... indicates the star was not observed. If B/R ratio is > 1 the emission wings indicate inflow, if B/R ratio is < 1 the emission wings indicate outflow.

Table 5. Physical Parameters of Cluster Members in M13

ID No.	$M_V$	$(B - V)_0$	$(V - K)_0$	P <sup>a</sup>	$T_{eff}$ (K)	$\log L/L_\odot$	$R/R_\odot$
III-65	+0.74	0.80	2.095	99	5010	1.750	9.7
K188	-1.09	1.03	2.635	99	4470	2.575	31.5
K210	-0.15	0.86	2.305	99	4790	2.138	16.6
K220	+0.50	0.74	2.095	99	5010	1.846	10.8
K223	+0.23	0.83	2.165	99	4900	1.964	13.0

<sup>a</sup>Membership probability from proper motion observations (Cudworth & Monet 1979).

Note. — This table is available in its entirety in a machine-readable form in the on-line journal. A portion is shown here for guidance regarding its form and content.

Table 6. Physical Parameters of Cluster Members in M92

ID No.	$M_V$	$(B - V)_0$	$(V - K)_0$	P <sup>a</sup>	$T_{eff}$ (K)	$\log L/L_\odot$	$R/R_\odot$
I-14	+0.10	0.71	2.093	99	4980	2.006	13.5
I-40	+0.14	0.71	2.085	99	4990	1.989	13.2
I-67	-1.32	0.90	2.499	99	4570	2.640	33.4
I-68	-0.03	0.73	1.894	99	5240	2.033	12.6
II-6	+0.50	0.73	2.093	99	4980	1.846	11.3

<sup>a</sup>Membership probability from proper motion observations (Cudworth 1976).

Note. — This table is available in its entirety in a machine-readable form in the on-line journal. A portion is shown here for guidance regarding its form and content.

Table 7. Radial and H $\alpha$  Bisector Velocity of Observed Stars in M13

ID No.	$v_{rad,1}^a$ (km s $^{-1}$ )	$v_{rad,2}^a$ (km s $^{-1}$ )	$v_{rad,3}^a$ (km s $^{-1}$ )	$v_{rad,4}^a$ (km s $^{-1}$ )	$v_{bis,1}^b$ (km s $^{-1}$ )	$v_{bis,2}^b$ (km s $^{-1}$ )
III-65	$-246.0 \pm 0.4$	...	$-245.9 \pm 0.2$	...	$+0.5 \pm 2.5$	...
K188	$-244.9 \pm 0.3$	...	$-245.2 \pm 0.2$	...	$-1.4 \pm 1.0$	...
K210	$-250.8 \pm 0.2$	...	$-249.9 \pm 0.3$	...	$-0.0 \pm 0.6$	...
K220	$-244.0 \pm 0.3$	$-243.6 \pm 0.2$	...	$-242.9 \pm 0.2$	$+0.4 \pm 1.4$	$+1.5 \pm 0.7$
K223	...	$-242.6 \pm 0.2$	...	$-242.0 \pm 0.2$	...	$+0.2 \pm 0.9$

<sup>a</sup>Observations: 1: 2006 March 14 (H $\alpha$ ), 2: 2006 May 10 (H $\alpha$ ), 3: 2006 March 16 (RV31), 4: 2006 May 10 (RV31).

<sup>b</sup>Observations: 1: 2006 March 14; 2: 2006 May 10.

Note. — This table is available in its entirety in a machine-readable form in the on-line journal. A portion is shown here for guidance regarding its form and content.

Table 8. Radial and H $\alpha$  Bisector Velocity of Observed Stars in M92

ID No.	$v_{rad,1}^a$ (km s $^{-1}$ )	$v_{rad,2}^a$ (km s $^{-1}$ )	$v_{rad,3}^a$ (km s $^{-1}$ )	$v_{bis,1}^b$ (km s $^{-1}$ )	$v_{bis,2}^b$ (km s $^{-1}$ )
I-14	$-124.2 \pm 0.3$	$-124.0 \pm 0.2$	$-123.9 \pm 0.2$	$-0.5 \pm 1.2$	$+0.6 \pm 0.5$
I-40	$-125.2 \pm 0.2$	...	$-124.6 \pm 0.2$	$+0.5 \pm 0.5$	...
I-67	$-120.9 \pm 0.2$	...	$-120.2 \pm 0.2$	$-1.8 \pm 0.4$	...
I-68	...	$-129.7 \pm 0.2$	...	...	$+0.0 \pm 0.6$
II-6	$-122.6 \pm 0.3$	$-123.1 \pm 0.3$	$-121.8 \pm 0.2$	$+2.5 \pm 0.7$	$-1.8 \pm 0.8$

<sup>a</sup>Observations: 1: 2006 May 7 (OB25), 2: 2006 May 9 (OB25), 3: 2006 May 7 (RV31)

<sup>b</sup>Observations: 1: 2006 March 14; 2: 2006 May 10.

Note. — This table is available in its entirety in a machine-readable form in the on-line journal. A portion is shown here for guidance regarding its form and content.

Table 9. B/R ratio of Ca II K Line for Stars Showing Emission in M13 and M92

ID No.	M13		ID No.	M92	
	<i>B/R</i> 2006 March 16	<i>B/R</i> 2006 May 10		<i>B/R</i> 2006 May 8	<i>B/R</i> 2006 May 9
K228	> 1	...	II-53	> 1	≈ 1
K422	≈ 1	≈ 1	III-65	> 1	...
K656	> 1	...	VII-10	≈ 1	≈ 1
L18	> 1	...	VII-18	< 1	< 1
L26	> 1	≈ 1	VII-39	< 1	...
L70	< 1	...	VII-122	> 1	...
L72	< 1	...	X-49	> 1	...
L95	...	> 1	XI-14	≈ 1	...
L96	< 1	...	XI-80	> 1	...
L109	> 1	...	XII-5	> 1	≈ 1
L140	> 1	...	XII-8	> 1	...
L158	≈ 1	...	XII-34	≈ 1	...
L169	< 1	...			
L199	< 1	...			
L250	≈ 1	...			
L252	> 1	...			
L316	> 1	...			
L345	...	> 1			
L384	...	< 1			
L403	> 1	...			
L414	< 1	...			
L423	≈ 1	...			
L465	> 1	...			
L549	≈ 1	...			
L598	≈ 1	...			
L745	≈ 1	...			
L773	> 1	...			
L835	≈ 1	...			
L863	> 1	...			
L954	< 1	...			
L973	< 1	...			
L1023	> 1	...			
L1043	≈ 1	...			
L1073	≈ 1	...			

Note. — The parameter *B/R* is the intensity ratio of Blue (short wavelength) and Red (long wavelength) emission peaks.

Table 10. Relative Radial Velocity of Ca II K central absorption.

M13		M92	
ID No.	$v_{rel}$ (km s <sup>-1</sup> )	ID No.	$v_{rel}$ (km s <sup>-1</sup> )
K228	+0.2 ± 0.8	II-53	-7.2 ± 0.9
K422	-3.2 ± 0.9	III-65	-10.9 ± 0.9
K656	-2.2 ± 0.7	VII-18	-13.0 ± 0.4
L18	-0.3 ± 0.8	VII-122	-6.6 ± 0.8
L26	-3.5 ± 0.9	X-49	-7.6 ± 1.0
L70	-10.2 ± 0.5	XII-8	-5.4 ± 0.8
L72	-10.0 ± 0.9		
L96	-14.7 ± 0.9		
L109	-7.8 ± 1.0		
L140	-0.6 ± 0.6		
L158	-7.1 ± 0.9		
L169	-6.4 ± 0.9		
L199	-10.8 ± 0.8		
L250	-12.8 ± 1.0		
L252	-1.4 ± 0.8		
L316	-6.1 ± 0.7		
L403	-1.6 ± 0.9		
L414	-12.0 ± 1.1		
L423	-5.2 ± 1.1		
L465	-6.3 ± 0.9		
L549	-3.7 ± 1.2		
L598	-7.2 ± 0.2		
L745	-8.7 ± 0.8		
L773	-3.9 ± 1.1		
L835	-11.5 ± 0.9		
L863	-4.0 ± 1.1		
L954	-9.8 ± 1.1		
L973	-11.0 ± 0.6		
L1023	-3.4 ± 1.1		
L1043	-0.8 ± 0.9		
L1073	-9.4 ± 1.0		

Note. — The table does not contain stars where the central absorption was not visible in the spectrum.



Table 11. Characteristics of Emission in Four Clusters

Cluster	[Fe/H] <sup>a</sup>	$\log(L/L_{\odot,H\alpha,1})^b$	$\log(L/L_{\odot,H\alpha,2})^c$	$\log(L/L_{\odot,Ca\ II\ K})^d$	No. <sup>e</sup>	$P_1^f$	$P_2^g$
M13	−1.54	1.95	2.79	1.92	123	45	78
M15	−2.26	2.36	2.78	2.36	110	22.5	83
M92	−2.28	2.05	2.74	1.96	64	18	78
NGC 2808 <sup>h</sup>	−1.15	2.5	2.5	2.60	137	7	52

<sup>a</sup>Harris (1996).

<sup>b</sup>The luminosity limit of all stars showing emission in H $\alpha$ .

<sup>c</sup>The luminosity limit of only RGB stars showing emission in H $\alpha$ .

<sup>d</sup>The luminosity limit of all stars showing emission in Ca II K.

<sup>e</sup>Number of stars observed.

<sup>f</sup>The percentage of stars from all observations showing outflow in H $\alpha$  emission wing asymmetry.

<sup>g</sup>The percentage of stars from all observations showing H $\alpha$  emission above  $\log(L/L_{\odot,H\alpha,2})$ .

<sup>h</sup>Parameters of NGC 2808 for the RGB stars were measured by Cacciari et al. (2004). No AGB stars in that sample are well-separated on the CMD. Thus the RGB limit marks the faint limit for all stars in the cluster.